Engineering 11 (2022) 42–59

Contents lists available at ScienceDirect

Engineering

journal homepage: www.elsevier.com/locate/eng

Research
Advanced Antennas for Wireless Connectivity—Review

High Performance Electrically Small Huygens Rectennas Enable Wirelessly Powered Internet of Things Sensing Applications: A Review

Wei Lin *, Richard W. Ziolkowski *

Global Big Data Technologies Centre, School of Electrical and Data Engineering, University of Technology Sydney, Ultimo, NSW 2007, Australia

ARTICLE INFO

Article history:
Received 4 January 2021
Revised 10 June 2021
Accepted 8 August 2021
Available online 22 December 2021

Keywords:
Antenna
Array
Cardioid pattern
Electrically small antenna
Huygens dipole antenna
Internet of Things (IoT)
Rectenna
Rectifier circuit
Wireless power transfer

ABSTRACT

Far-field wireless power transfer (WPT) is a major breakthrough technology that will enable the many anticipated ubiquitous Internet of Things (IoT) applications associated with fifth generation (5G), sixth generation (6G), and beyond wireless ecosystems. Rectennas, which are the combination of rectifying circuits and antennas, are the most critical components in far-field WPT systems. However, compact application devices require even smaller integrated rectennas that simultaneously have large electromagnetic wave capture capabilities, high alternating current (AC)-to-direct current (DC) (AC-to-DC) conversion efficiencies, and facilitate a multifunctional wireless performance. This paper reviews various rectenna miniaturization techniques such as meandered planar inverted-F antenna (PIFA) rectennas; miniaturized monopole- and dipole-based rectennas; fractal loop and patch rectennas; dielectric-loaded rectennas; and electrically small near-field resonant parasitic rectennas. Their performance characteristics are summarized and then compared with our previously developed electrically small Huygens rectennas that are proven to be more suitable for IoT applications. They have been tailored, for example, to achieve battery-free IoT sensors as is demonstrated in this paper. Battery-free, wirelessly powered devices are smaller and lighter in weight in comparison to battery-powered devices. Moreover, they are environmentally friendly and, hence, have a significant societal benefit. A series of high-performance electrically small Huygens rectennas are presented including Huygens linearly-polarized (HLP) and circularly-polarized (HCP) rectennas; wirelessly powered IoT sensors based on these designs; and a dual-functional HLP rectenna and antenna system. Finally, two linear uniform HLP rectenna array systems are considered for significantly larger wireless power capture. Example arrays illustrate how they can be integrated advantageously with DC or radio frequency (RF) power-combining schemes for practical IoT applications.

1. An introduction to wireless power transfer (WPT) technologies for Internet of Things (IoT) applications

WPT technologies enable the transfer of electromagnetic (EM) energy from a power source to the load of an electronic device without any conducting wires or physical contact. WPT is much safer and more reliable than conventional wire-powered systems, in particular, for application in industrial activities such as mining and gas exploration. Moreover, WPT has become extremely important for the current and future IoT systems associated with the rapid developments of fifth generation (5G), sixth generation (6G) and beyond wireless technologies. Future ubiquitous wirelessly powered IoT devices are anticipated to negate the current need for short-life, bulky, and non-degradable chemical batteries. WPT is a highly attractive green-technology that has attracted considerable attention from both industry and the academic worlds.

The concept of WPT can be traced back to Nikola Tesla's experiments at the end of the 19th century [1–3]. He invented the first resonant inductive near-field WPT technique and successfully lit a lamp bulb wirelessly. Far-field WPT has a long history dating back to the 1960s. Several very nice reviews of the past and recent developments are available [4–18]. Solar power satellites (SPSs) and wirelessly powered aircraft and high altitude platforms are examples of very long distance applications of WPT technology. With the much deeper and faster development of both science and engineering in applied electromagnetics in the 21st century, WPT technology has already been widely adopted in many commercial electronics products, such as wireless-chargeable

* Corresponding authors.
E-mail addresses: Wei.Lin@uts.edu.au (W. Lin), Richard.Ziolkowski@uts.edu.au (R.W. Ziolkowski).

https://doi.org/10.1016/j.eng.2021.08.025
2095-8099/

Apple™ products, electric toothbrushes, radio frequency identification (RFID) systems, and electric cars.

Based on their distinctive operating mechanisms, WPT systems can be categorized into two major types: near-field [19] and resonant mid-range [20–22] magnetically-coupled systems, and far-field EM-wave power transfer systems. The magnetically-coupled systems have generally adopted coils to transfer energy via magnetic fields. The physics of these systems enables only short-distance WPT. The sole approach that enables long-distance WPT, as far as hundreds of meters up to thousands of kilometers, is the transmission and reception of the power carried by propagating EM waves. Fig. 1 illustrates the power flow diagram associated with a typical far-field WPT system facilitated by EM waves. The transmitting antenna emits the EM waves that are energized from an alternating current (AC) power source. A receiver located in the far field of the transmitting antenna captures the emitted EM waves and converts that AC captured energy into direct current (DC) power via a rectifier circuit. The longest realized WPT has been from a space satellite; the satellite's solar panels collected sunlight (EM waves) and its microwave transmitters beamed that energy to the Earth's surface to be captured by a rectenna array, i.e., an SPS system [5,23].

Far-field WPT is the major enabling technology for realizing battery-free IoT ecosystems in the incoming 5G and future wireless generations [14]. WPT opportunities now widely exist owing to the recent significant advances in ultra-low power electronics. For example, a battery-free cellphone powered solely by wireless fildelity (WiFi) signals has been successfully demonstrated [24]. Moreover, it has been concluded [25] that the power consumption of many IoT sensors can reach less than 0.1 milliwatts, which means that WPT base stations would be able to broadcast at very low power levels. Fig. 2 illustrates an application example of a wirelessly powered IoT sensing system for smart agriculture and farming. Many IoT sensors can be deployed around a single transmitter (power beacon) which itself is powered by a renewable energy source. It is an environmental-friendly arrangement that requires significantly less human intervention and labor. This type of battery-free ecosystem will help increase agricultural productivity and quality. The automatically collected data from the IoT sensors is transmitted by them back to the base station which also acts as the data gateway. The data would include important information vital to crops such as the soil pH level, moisture level, temperature, and humidity. It can then be analyzed for optimal decision making, for example, when to plant and when to harvest. Given the large number of anticipated IoT sensors and the current battery costs and sizes associated with this application, far-field WPT technology is highly desired for future smart agriculture and other wireless sensor networks.

2. Miniaturized rectenna designs for far-field WPT

The most critical aspect of a WPT-enabled IoT system is the performance of its rectennas, i.e., the integration of the receiving antennas and their rectifier circuits. While numerous studies on rectenna designs have been published, such as those on multi-band rectennas [26], multi-port rectennas [27], low input-power designs [28,29], rectenna arrays [30,31], and metasurface-based designs [17,32,33], these systems are not suitable for battery-free IoT devices and large numbers of elements in applications such as sensor networks because of their large sizes. Specifically, their ka values are larger than 1, where k is the free-space wavenumber and a is the smallest sphere that encloses the entire rectenna. Note that a design is considered to be electrically small if $ka \leq 1$.

Several miniaturization techniques have been developed to achieve much more compact rectenna designs. These are summarized in Table 1 [24,34–38]. The meandered planar inverted-F antenna (PIFA)-based rectennas are one of the most popular designs [24,39–41]. The concept is to bend the arm of the receiving PIFA to realize size miniaturization. For example, a meandered PIFA rectenna was adapted in Ref. [24] to achieve a wirelessly-powered cell phone. Although the size was reduced in comparison to conventional PIFA or dipole-based rectennas, its wireless power capture capability was limited because the radiation pattern of the receiving antenna is omnidirectional with a low realized gain. Moreover, its polarization purity was low. Another miniaturization technique includes the design of meandered monopole- or dipole-based rectennas [34,42,43]. Although these designs achieve a higher polarization purity compared to the PIFA-based designs, their realized gains are still low and their sizes are not electrically small. Moreover, it is clear from Table 1 that it is difficult to seamlessly integrate these designs with the rectifier circuit. To address this issue, a fractal loop rectenna was developed in Ref. [35]. The entire system was very compact because the rectifier circuit was integrated inside the receiving loop antenna. Nonetheless, its wireless power capture capability was still low as a result of the low-gain omnidirectional pattern of its receiving loop antenna. To enhance the wireless power capture capability, i.e., to attain a higher realized gain of the receiving antenna, miniaturized fractal patch-based rectennas were developed in Refs. [36,44,45]. Although the area of each patch was reduced, the realized gain of the receiving antenna remained dependent on the size of the ground plane. Thus, the overall size of these designs remained large. To further reduce the rectenna size, dielectric-loaded versions were developed in Refs. [37,46,47]. However, their wireless power capture capability decreased owing to the dielectric loading, and their sizes were still not electrically small. One rectenna design in Ref. [38] achieved an electrically small size. However, the radiation pattern of its receiving antenna was omnidirectional with only a 1.0 decibel (dB) peak realized gain.

All of these "miniaturized" rectenna designs remain unsuitable for the targeted IoT applications. They do not simultaneously meet the associated challenges of being very compact in size, having large and broad-angle wireless EM wave capture capabilities, and having high AC-to-DC conversion efficiencies, while also being easy to fabricate and assemble with low costs.

As will be demonstrated in this paper, these challenges have been successfully met with the development of a series of high-performance electrically small Huygens rectenna systems that enable wirelessly powered IoT applications. The electrically small Huygens linearly-polarized (HLP) rectenna systems are presented first. Their design methodology smartly integrates two

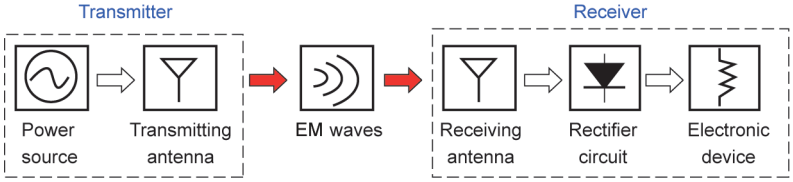

Fig. 1. Far-field WPT facilitated by EM waves, antennas, and rectifiers.

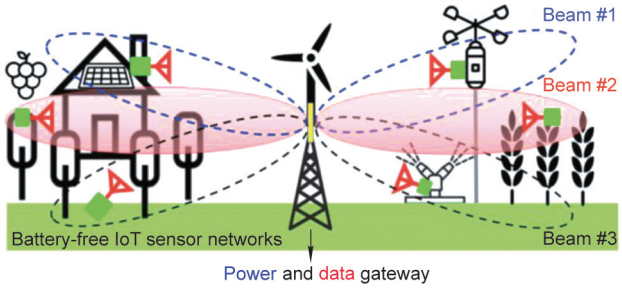

Fig. 2. Application example: wirelessly powered IoT sensing system for smart agriculture and farming.

metamaterial-inspired electrically small radiating near-field resonant parasitic (NFRP) elements: the Egyptian axe dipole (EAD) and the capacitively-loaded loop (CLL), which are excited by an elemental, driven radiating element into a highly compact entity [48,49]. The Huygens cardioid radiation patterns are obtained by achieving balanced, in-phase radiated electric, and magnetic fields. A low-profile HLP version is realized using three printed circuit board (PCB) substrate layers. An ultrathin HLP system is realized on a single PCB substrate [50]. The seamless integration of both electrically small antennas with IoT temperature and light sensors has been accomplished and confirmed with measured prototypes [51]. Two electrically small Huygens circularly-polarized (HCP) rectenna systems that address polarization mismatch issues are then described. One version is a low-profile HCP rectenna again realized with three PCB substrate layers [52]. The other is a modified HCP rectenna realized with four PCB substrate layers that achieves the maximum AC-to-DC conversion efficiency [53]. A dual-functional HLP rectenna and antenna system that is capable for both WPT and communications functions is discussed [54]. It meets the needs of emerging applications, such as wirelessly powered sensors, that require simultaneous wireless information and power transfer (SWIPT) performance. Finally, two HLP rectenna array systems are developed to further enhance the capture of available wireless power. Both the DC and radio frequency (RF) power-combining schemes are described.

The remainder of this paper is organized as follows. Section 3 illustrates the design methodology of the electrically small Huygens rectennas. Section 4 introduces the two HLP rectenna systems and how they are tailored and integrated effectively with IoT temperature and light sensors. Section 5 presents the two HCP rectenna systems that can be similarly tailored for sensor and other IoT applications. Section 6 discusses the dual-functional HLP rectenna and antenna system. Section 7 demonstrates rectenna arrays that facilitate both RF and DC combining schemes. Finally, Section 8 is the conclusion. All numerical simulations and their optimizations reported herein were performed using the commercial software: Advanced Design System (ADS, Keysight Technologies, Inc., USA), ANSYS Electromagnetics Suite (HFSS, ANSYS, USA), and CST

Table 1
Typical examples of miniaturized rectenna designs.

Meandered PIFA rectenna [24]	Meandered monopole/dipole rectenna [34]	Fractal loop rectenna [35]
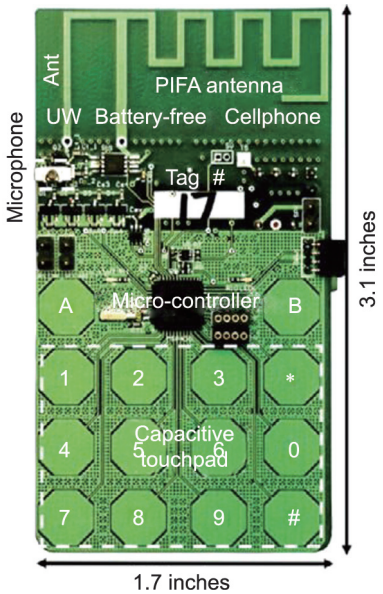	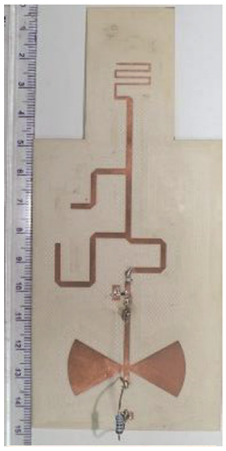	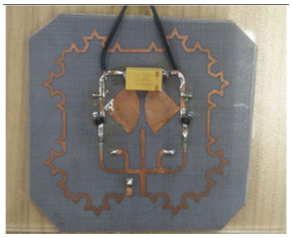
Fractal patch rectenna [36]	**Dielectric-loaded rectenna [37]**	**Electrically small near-field resonant parasitic rectenna [38]**
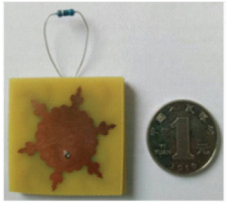	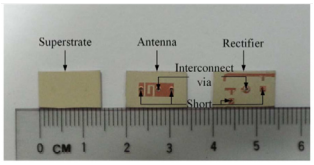	

The figure of meandered PIFA rectenna is reproduced from Ref. [24] with permission of ACM, ©2017. The figure of fractal loop rectenna is reproduced from Ref. [35] with permission of IEEE, ©2017. The figure of dielectric-loaded rectenna is reproduced from Ref. [37] with permission of IEEE, ©2014. The figure of electrically small near-field resonant parasitic rectenna is reproduced from Ref. [38] with permission of AIP Publishing, ©2011.

Studio Suite (CST, Germany). The reported simulation model results employed the known, real properties of all of the dielectrics and conductors.

3. Design methodology of electrically small Huygens rectennas

The rectennas presented herein are composed of Huygens dipole antennas (HDAs) and ultracompact rectifier circuits. The basic EM concepts associated with electrically small HDAs are presented first to understand the underlying design methodologies. The associated rectifier circuits and layouts are then described.

3.1. Electromagnetics of electrically small Huygens antennas

The basic HDA consists of a pair of complementary radiating elements, for example, an electric dipole (ED) and a magnetic dipole (MD). If the two dipoles are arranged orthogonal to each other and radiate in-phase balanced fields, a cardioid-shaped Huygens pattern will be realized as shown in Fig. 3(a). While the basic electromagnetics of a Huygens antenna is the same as the magnetoelectric (ME) dipole antennas that have been invented and extensively developed by Luk and Wong [55], Ge and Luk [56], Luk and Wu [57], Wang et al. [58], and Li et al. [59], they achieve it with significantly more compact structures. For example, the entire volume of our developed HLP receiving antenna ($\pi(0.115\lambda_0)^2 \times 0.04\lambda_0 = 0.00166\lambda_0^3$, where λ_0 is the wavelength of the resonance frequency) [49] is 150 times smaller than the volume ($\lambda_0 \times \lambda_0 \times 0.25\lambda_0 = 0.25\lambda_0^3$) of the original half-wavelength ME dipole design in Ref. [55]. Although the bandwidth of that ME dipole (43.8%) is much larger, our narrowband electrically small design (~0.6%) is more suitable for WPT applications that do not require a wide bandwidth. The gain of the ME dipole (8 dBi) is higher simply because it has a large ground plane and, hence, a notably larger overall size. On the other hand, the half-power beamwidth of our HLP antenna (> 150°) is significantly larger.

Fig. 3(a) presents the ideal HDA. An infinitesimal ED is oriented along the +*x*-axis. An infinitesimal MD is oriented orthogonal to it along the +*y*-axis. The far-field expressions for their electric fields, $\vec{E}_{ED}$ and $\vec{E}_{MD}$, are [60]

$$\begin{aligned}\vec{E}^{ff}_{ED} &= +jk\eta[I_eL]\cdot\frac{e^{-jkr}}{4\pi r}\cdot[\hat{r}\times\hat{r}\times\hat{x}]\\ &= +jk\eta\,[I_eL]\cdot\frac{e^{-jkr}}{4\pi r}\cdot\left[-\cos\theta\cos\varphi\,\hat{\theta}+\sin\varphi\,\hat{\varphi}\right]\end{aligned} \tag{1}$$

$$\begin{aligned}\vec{E}^{ff}_{MD} &= +jk\,[I_mL]\cdot\frac{e^{-jkr}}{4\pi r}\cdot[\hat{r}\times\hat{y}]\\ &= +jk\,[I_mL]\cdot\frac{e^{-jkr}}{4\pi r}\cdot\left[-\cos\varphi\,\hat{\theta}+\cos\theta\sin\varphi\,\hat{\varphi}\right]\end{aligned} \tag{2}$$

where θ is the elevation angle relative to the *z*-axis; φ is the angle in the azimuth *x*–*y* plane; *r* is the distance from the origin to the

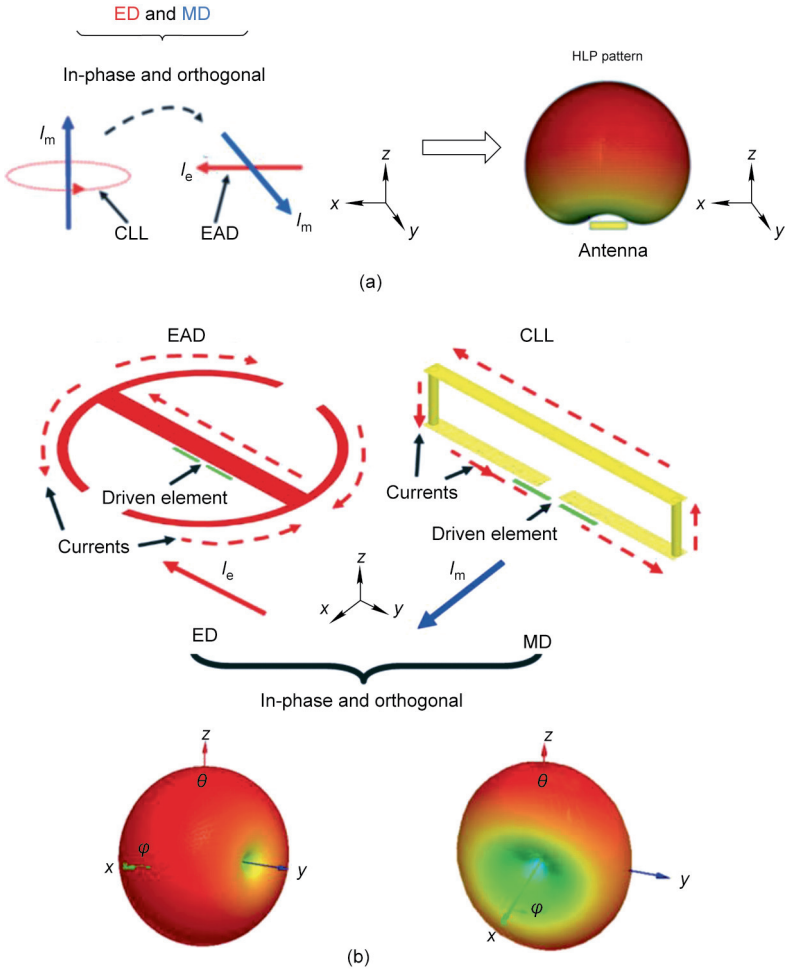

Fig. 3. HLP antenna. (a) Basic EM configuration and broadside radiated three-dimensional (3D) cardioid pattern; (b) dipole antenna designs realized with electrically small NFRP elements, each excited by a driven elemental dipole antenna. I_m: the magnetic current; I_e: the electric current; φ: the azimuth angle relative to the *x*-axis in the *x*–*y* plane; θ: the elevation angle relative to the *z*-axis.

observation point; I_m is the magnetic current; I_e is the electric current; L is the length of the electric and magnetic current elements; I_eL is the ED current moment; I_mL is the MD current moment; $k = 2\pi/\lambda_0$ is the free-space wavenumber, λ_0 being the free-space wavelength corresponding to its resonance frequency; and $\eta = \sqrt{\mu_0/\varepsilon_0}$ is the free-space wave impedance where μ_0 and ε_0 are the permeability and permittivity of free space, respectively. The total field radiated by both dipoles in concert is the sum of the fields they radiate individually. With I_e and I_m being orthogonal and in-phase, the balanced condition: $I_m = \eta I_e$, yields the Huygens far-field radiation pattern:

$$\vec{E}^{\,ff}_{ED} + \vec{E}^{\,ff}_{MD} = jk\eta\,[I_eL]\frac{e^{-jkr}}{4\pi r}\,(1+\cos\theta)\left[-\cos\varphi\hat{\theta} + \sin\varphi\hat{\varphi}\right] \qquad (3)$$

As illustrated, a cardioid behavior is attained with this HDA concept, i.e., the factor $(1 + \cos\theta)$ yields a factor of two in the broadside direction, θ = 0°, and zero in the opposite one, θ = 180°. Notably, the patterns in both principal vertical planes, φ = 0° and φ = 90°, are identical. The peak directivity of the HDA is twice that of either dipole element individually and its front-to-back ratio (FTBR) is infinite instead of being unity as it is for each dipole individually as illustrated in Fig. 3(b).

The metamaterial-inspired electrically small NFRP elements, the EAD and the CLL, are ideal candidates for the ED and MD, respectively [61], to realize a practical electrically small HDA [48–54]. As illustrated in Fig. 3(b), the EAD functions as an ED and the CLL acts as an MD, both of which individually have a donut-shaped omnidirectional three-dimensional (3D) radiation pattern. If they are seamlessly integrated and properly balanced to yield the behavior described by Eq. (3), the Huygens cardioid radiation pattern in Fig. 3(a) is realized. Note that the dipole directions are purposely rotated by 90° in Fig. 3(b) from those in Fig. 3(a), i.e., the ED is now oriented along the $-y$-axis and the MD is oriented along the $+x$-axis. This choice emphasizes that in both Figs. 3(a) and (b), the cross-product of the ED and MD directions is along the $+z$-axis, the direction of the maximum of the cardioid pattern. The practical realization of this Huygens behavior will be demonstrated in the configuration shown in the figure below in Section 4.1. The actual realizations of an HDA with these metamaterial-inspired NFRP elements that was achieved in practice with low-cost PCB technology is described in the next section.

3.2. Compact rectifier circuit design

The other critical part of an electrically small rectenna is the rectifier circuit. It must be compact and highly efficient. Fig. 4 presents the circuit model of the two-diode full-wave rectifier developed in Ref. [49]. The main components of the rectifier are the two Schottky diodes arranged in a parallel configuration. An inductor L and the two capacitors C_1 and C_3 form an input impedance matching network for a standard 50 Ω source. The inductor also acts as a high-stop filter to reflect back any higher-order harmonics generated by the nonlinear diodes. Capacitor C_2 also acts as an energy storage device during one half-cycle. The vertical diode facilitates charging it during each negative portion of the sinusoidal signal. This stored energy is released during the positive portion, which doubles the output voltage. The capacitor C_3 smooths the output DC voltage delivered to the load, represented by the resistor R_L.

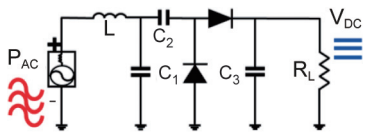

Fig. 4. Circuit model of an ultracompact and highly efficient rectifier. P_{AC}: AC power; V_{DC}: DC voltage; L: inductor; R_L: load resistor; C_1, C_2, and C_3: capacitors.

The rectifier circuit is easily realized on a compact PCB substrate as shown in Fig. 5.

Because the circuit is realized as a parallel microstrip line structure, the thickness of the PCB is not important and can be ultrathin. Our targeted operating frequency is in the free 915 MHz industrial, scientific, and medical (ISM) band. For optimal operation in this band, HSMS286C Schottky diodes (Broadcom Inc., USA) were selected. The inductors, including two RF chokes (L_{RF_choke}), were added to prevent any AC signals arising from the twin-line transmission line from coupling with the DC output. The capacitors were from Murata Manufacturing Co., Ltd., Japan and the resistor R_L was obtained from Yageo, China. All of these lumped components were in 0403 (1 mm length) surface-mount device (SMD) packages. The optimized values for each component were: L = 39 nH, C_1 = 0.4 pF, C_2 = 100 pF, C_3 = 100 pF, R_L = 10 kΩ, and L_{RF_choke} = 560 nH. The PCB implementation of the rectifier is compact with its length being only 7.3 mm.

Fig. 6 [49] presents the measured performance of the rectifier [49]. The input parallel microstrip line of the rectifier was connected to a differential source that is realized by a balun-choked coaxial cable. The cable was connected to a signal generator from Keysight Technologies, Inc., USA. Fig. 6(a) [49] shows the measured magnitude of the S-parameter S_{11}, $|S_{11}|$, values as a function of the source frequency under different input power levels. The 10 dB impedance bandwidth covers 120 MHz, from 825 to 945 MHz for a variety of input power levels.

Fig. 6(b) [49] presents the measured and simulated AC-to-DC efficiencies as functions of the input power at our targeted 915 MHz frequency. The AC-to-DC conversion efficiency is defined as the output DC power divided by the input RF/AC power. The measured results agree well with their simulated values. The measured peak AC-to-DC efficiency was 80.3% for a 10 dBm (10 mW) input power, which is very close to the simulated peak value of 81.8%. Moreover, the efficiency is greater than 50% when the input power ranges widely from −5 dBm (0.3 mW) to 13.5 dBm (22.4 mW). Thus, the developed compact rectifier circuit demonstrated a high AC-to-DC conversion efficiency. The small discrepancy in the received power level for the peak efficiency value is due to the difference between the actual parameters of the real HSMS286C diodes and those values used in the ADS simulation model. Note that the matching inductor L in this circuit introduces a nontrivial loss to the system. As shown in our other designs below, the AC-to-DC conversion efficiency of this rectifier can be further improved if the inductor L is removed and its absence is properly counterbalanced by the input impedance of the antenna.

4. Highly efficient, electrically small HLP rectennas

Two measured, highly efficient, electrically small HLP rectennas are discussed. Their simulated and measured results are presented.

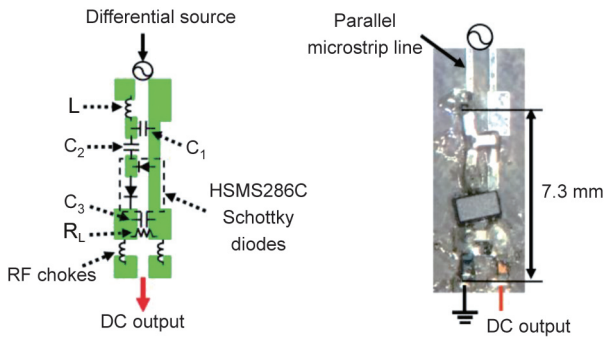

Fig. 5. Implementation on the compact rectifier circuit on a thin PCB substrate.

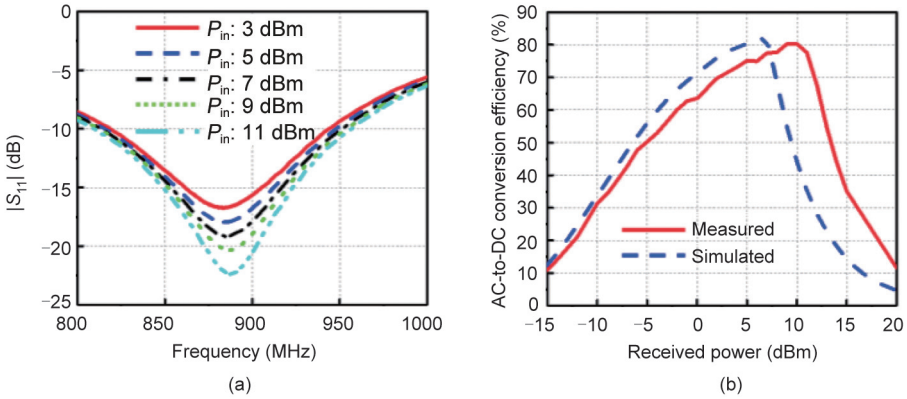

Fig. 6. (a) Measured $|S_{11}|$ as a function of the source frequency under different input power. P_{in}: the input power. (b) Measured and simulated AC-to-DC conversion efficiencies of the rectifier as functions of the received power. Reproduced from Ref. [49] with the permission of the IEEE, ©2019.

Their practical versions tailored to realize wirelessly powered temperature and light IoT sensors are described in detail.

4.1. Low-profile HLP rectenna realized with three PCB substrate layers

The presented design methodology was used to realize a low-profile electrically small HLP rectenna implemented with low-cost PCB technology [49]. Its simulation models are shown in Fig. 7 [49]. The entire rectenna consists of three PCB disks as depicted in Fig. 7(a) [49]. Each layer was realized as a Rogers Duroid™ 5880 copper-clad substrate. Its relative permittivity, permeability, and loss tangent are 2.2, 1.0, and 0.0009, respectively. The thickness of Substrate #1 and Substrate #3 is 0.787 mm and that of Substrate #2 is 0.508 mm. The metallic traces of the EAD element are etched on the center Substrate #2, and the CLL is formed by two metallic strips connected by two vertical copper posts. One strip is printed on the upper surface of Substrate #1 and the other is printed on the upper surface of Substrate #3. As shown in Fig. 7(b) [49], the short-driven dipole and the metallic traces of the rectifier are seamlessly integrated and etched on the bottom surface of Substrate #3. The gap between Substrate #1 and Substrate #2 determines the coupling between the EAD and the CLL NFRP elements and, thus, the realization of the receiving antenna's Huygens cardioid pattern. It was optimized to be 4.0 mm in this design. The diameter of the HLP rectenna is only $0.23\lambda_0$ and its profile is only $0.04\lambda_0$. It is electrically small with its *ka* value being 0.723.

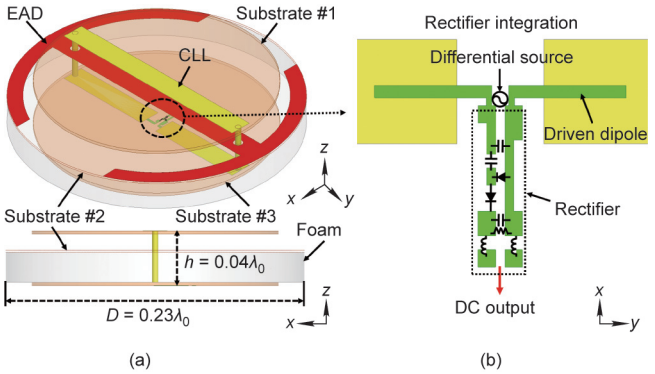

Fig. 7. Low-profile electrically small HLP rectenna realized with three PCB substrate layers. (a) Entire rectenna model. *h*: the height between the top of the lower conductor and the bottom of the upper conductor; *D*: the diameter of the substrate. (b) Details of the rectifier seamlessly integrated with its dipole antenna. Reproduced from Ref. [49] with the permission of the IEEE, ©2019.

Another significant feature of this design is the aforementioned absence of the lossy inductor in the rectifier. It was eliminated by properly tuning the input impedance of the broadside-radiating HLP antenna. This was achieved by adjusting the length of its elemental dipole antenna to have an inductive value that is directly matched to the rectifier, which has a capacitive impedance. Fig. 8(a) [49] presents the simulated impedance of the HLP antenna (without the rectifier) as a function of the source frequency. The impedance has an inductive value of (77 + j129) Ω at the targeted frequency of 915 MHz. Fig. 8(b) [49] shows the simulated radiation patterns at 915 MHz. It is clear that cardioid-shaped Huygens patterns are realized. The peak broadside gain is 3.8 dBi and a significantly high FTBR, 23.5 dB, is obtained. Broad and similar realized gain patterns in both principal vertical planes are obtained. The radiation efficiency of the antenna is 80%. Notably, while the ideal HDA has identical patterns in both principal vertical planes, the realistic system has slightly different ones simply because of the finite, different sizes of its elements in those planes.

Fig. 9 [49] presents the current distributions and directions on the EAD and CLL radiators over a period of time, *T*, at 915 MHz. They clearly demonstrate the resonant behavior of this NFRP element pair. The currents on the CLL (MD) element are the strongest at the times: $t = 0$ and $t = (2/4)T$. The currents on the EAD (ED) element are dominant at the times: $t = (1/4)T$ and $t = (3/4)T$. Because the phase of the equivalent MD is 90° ahead of its corresponding loop currents, the ED and MD are in-phase. As the NFRP elements are already orthogonal to one another by construction, the conditions for producing balanced fields; and, hence, the desired Huygens radiation performance was satisfied.

The fabricated HLP rectenna prototype is shown in Fig. 10 [49]. It is noted that two short copper rods were attached to the short-driven dipole for tuning purposes after the prototype's dimensions were discovered to not be the specified values. The rectenna was measured in an anechoic chamber as shown in Fig. 11 [49]. The far-field WPT measurement setup consisted of a signal generator (Keysight Technologies, Inc., USA), a power amplifier (Mini-Circuits, USA), a standard wideband horn antenna as the transmitting antenna, a DC power supply, a multimeter, and several 50 Ω cables. The rectenna was located 1.2 m from the horn antenna's aperture in its far field at 915 MHz.

The AC-to-DC conversion efficiency was calculated using the Friis transmission equation to determine the power, P_r, received by the HLP antenna [62]:

$$\frac{P_r}{P_t} = G_t \times G_r \times \left(\frac{\lambda_m}{4\pi R}\right)^2 \tag{4}$$

where P_t is the power transmitted by the horn antenna; G_t is the gain of the horn antenna (7 dBi); G_r is the realized gain of the HLP

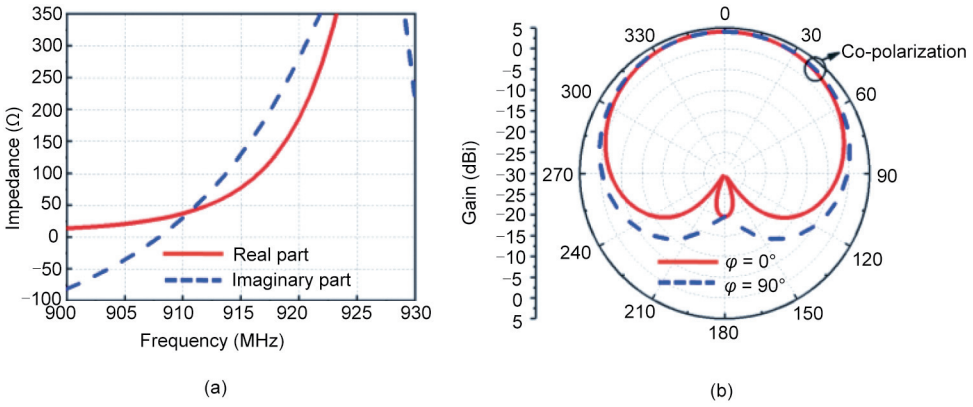

Fig. 8. Simulated performance characteristics of the HLP antenna. (a) Input impedance as a function of the source frequency; (b) realized gain patterns at 915 MHz in its two principal vertical planes. Reproduced from Ref. [49] with the permission of the IEEE, ©2019.

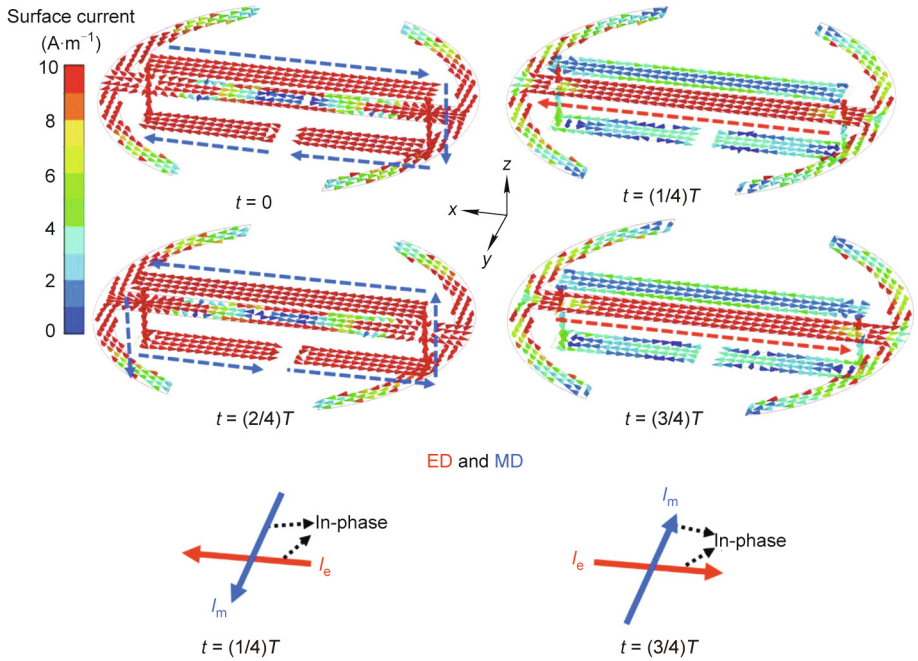

Fig. 9. Current distributions on the EAD and CLL NFRP elements during one source period in time, *T*. Reproduced from Ref. [49] with the permission of the IEEE, ©2019.

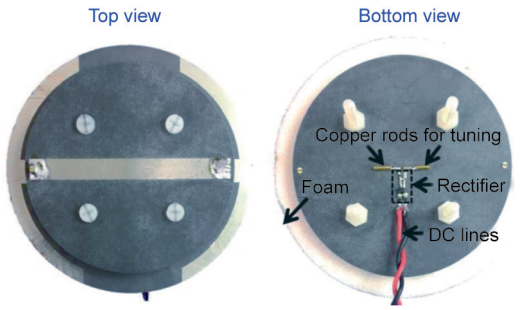

Fig. 10. Fabricated low-profile electrically small HLP rectenna. Reproduced from Ref. [49] with the permission of the IEEE, ©2019.

antenna (3.8 dBi); λ_m is the wavelength at the measured resonance frequency, 907 MHz (330.53 mm); and R is the distance between the horn antenna and the rectenna (1200 mm). The output DC voltage of the multimeter is labeled as V_o. The AC-to-DC conversion efficiency is then calculated as the ratio of the DC power measured at the load, V_0^2/R_L, and P_r.

Fig. 12 [49] presents the measured output DC voltage values and AC-to-DC conversion efficiencies of the rectenna and rectifier alone as functions of the received power at 907 MHz. The measured resonance frequency of the rectenna, 907 MHz, is only shifted by 8 MHz (0.87%) from the targeted 915 MHz. Moreover, because of the absence of the lossy inductor, the rectenna achieves a higher AC-to-DC conversion efficiency. The measured maximum AC-to-DC efficiency of the HLP rectenna reached 88.9% when the received power was 9.0 dBm, while the corresponding maximum of the rectifier alone was only 80.3%. Thus, the efficiency enhancement of 8.6% was obtained because the HLP antenna was designed to be matched directly to the rectifier. Notably, the efficiency is higher than 50% from the lower power level of −6 dBm (250 μW) to an even higher level of 13 dBm (20 mW). Thus, an input power range of nearly a factor of 100 was achieved.

One might ask why the measured conversion efficiency of the rectenna is greater than that of the rectifier attached to the inductor alone for the same received power. Careful inspection of Fig. 12(a) [49] indicates that the output voltage of the rectenna across the resistor load is greater than that of the rectifier plus

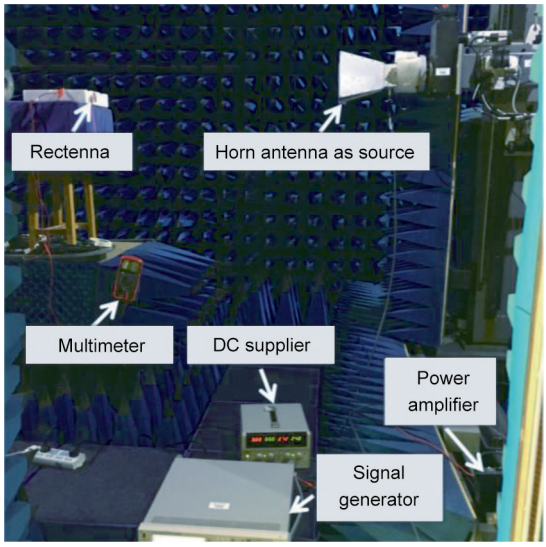

Fig. 11. The measurement setup for the far-field WPT rectennas. Reproduced from Ref. [49] with the permission of the IEEE, ©2019.

the inductor alone. This voltage difference, approximately 0.34 V (~5% difference), arises from the voltage drop that occurs across the lossy inductor which is necessary to match the rectifying circuit to the 50 Ω source. As previously indicated, this lossy inductor is purposely avoided in the same rectifying circuit when it is replaced with the HDA which was designed to be conjugately matched to it. Thus, the conjugate matching of the receiving antenna directly to the rectifying circuit without the lossy inductor maximizes the output voltage for the same received power. This leads to the higher output power of the rectifier and, hence, conversion efficiency attained by the rectenna.

The high EM-wave capture capacity of the HLP rectenna is illustrated with the CST simulation results shown in Fig. 13. An EM power flow comparison of the HLP system with a conventional half-wavelength dipole rectenna is presented. A plane-wave at 915 MHz is normally incident on both rectennas. The density of the power flow lines indicates the magnitude of the power carried by the EM waves in free-space. Despite the size of our rectenna being 2.5 times smaller than the conventional dipole one, it is clear that the wireless power capture area is significantly larger. The measured and simulation results confirm that the developed electrically small HLP rectenna achieves a very high AC-to-DC conversion efficiency because its HLP antenna has a very high wireless power capture capacity and its rectifying circuit is very efficient.

4.2. Ultrathin HLP rectenna realized with a single PCB substrate layer

Because it has its maximum realized gain in the broadside direction, the low-profile three-layer HLP rectenna is highly suitable for applications in which it would be attached on the surface of an object. However, its three layer design requires several fabrication steps. The ultrathin HLP rectenna developed in Ref. [50] was realized with only a single layer of the PCB substrate. This design is illustrated in Fig. 14 [50]. The EAD and CLL NFRP elements were printed on opposite sides of a single sheet of the Rogers Duroid™ 5880 copper-clad substrate. Its thickness of 0.508 mm makes it ultrathin at 915 MHz, being $\lambda_0/645$. The short driven dipole and the cascaded, integrated rectifier were placed on the same surface as the CLL element. The overall dimensions of the HLP rectenna are 99.5 mm × 38.0 mm × 0.508 mm ($0.304\lambda_0 \times 0.116\lambda_0 \times 0.0016\lambda_0$ at 915 MHz). The HLP antenna alone is 99.5 mm × 26.0 mm × 0.508 mm in size, i.e., the rectifier circuit length is 12.0 mm.

Fig. 15 [50] presents the simulated impedance and realized gain patterns of the HLP antenna. Its input impedance is once again designed to exhibit an inductive value to avoid the lossy inductor in the rectifier circuit. The input impedance at 915 MHz is (55 + j112) Ω. Reasonable Huygens cardioid patterns are observed with them being nearly identical in both principal vertical planes. The half-power beamwidth (HPBW) was 134° (±67°). Note that the fields are radiated with their maxima along the +z-axis. Consequently, its profile, $0.12\lambda_0$, is higher than that of the previous low-profile design ($0.04\lambda_0$). The peak realized gain is 4.6 dBi, which is 0.8 dBi higher than the three-layer HLP antenna design. This favorable enhancement occurs because there is less loss in this single-substrate design. Consequently, this single-layer HLP rectenna has a larger wireless power capture capacity than that of the lower profile three-layer version.

Fig. 16 [50] shows the fabricated ultrathin HLP rectenna, which is significantly lightweight and flexible. Fig. 17 [50] presents the measured and simulated performance characteristics of this rectenna. Fig. 17(a) [50] shows the simulated realized gain values of the HLP antenna and the measured output DC voltage of the rectenna system as functions of the source frequency. The measured peak output voltage (7.0 V) occurred at 909 MHz corresponding to the peak simulated realized gain value, which indicates only a slight 6 MHz (0.7%) shift from the simulated operating frequency of 915 MHz. It is electrically small with ka = 0.98 < 1.00. Fig. 17(b) [50] shows the measured output DC voltage values of the HLP rectenna, and the measured and simulated AC-to-DC conversion efficiencies of the rectenna and the rectifier circuit alone. The measured and simulated peak efficiency values were in very good agreement. The measured peak efficiency was 88% when

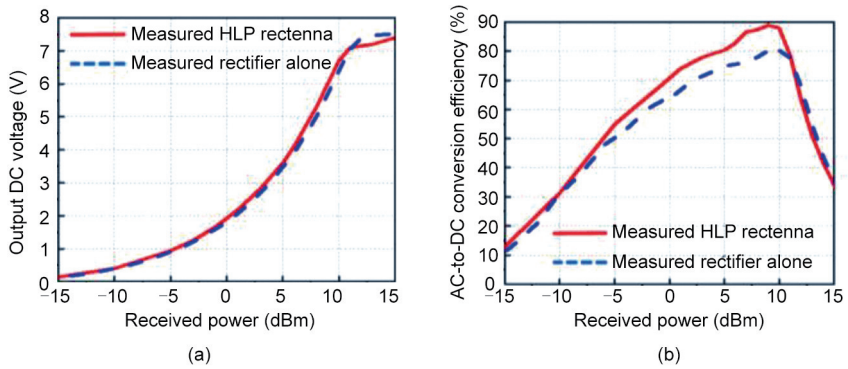

Fig. 12. Measured performance of the HLP rectenna and the rectifier alone at 907 MHz as a function of the received power. (a) Output DC voltage values; (b) AC-to-DC conversion efficiencies. Reproduced from Ref. [49] with the permission of the IEEE, ©2019.

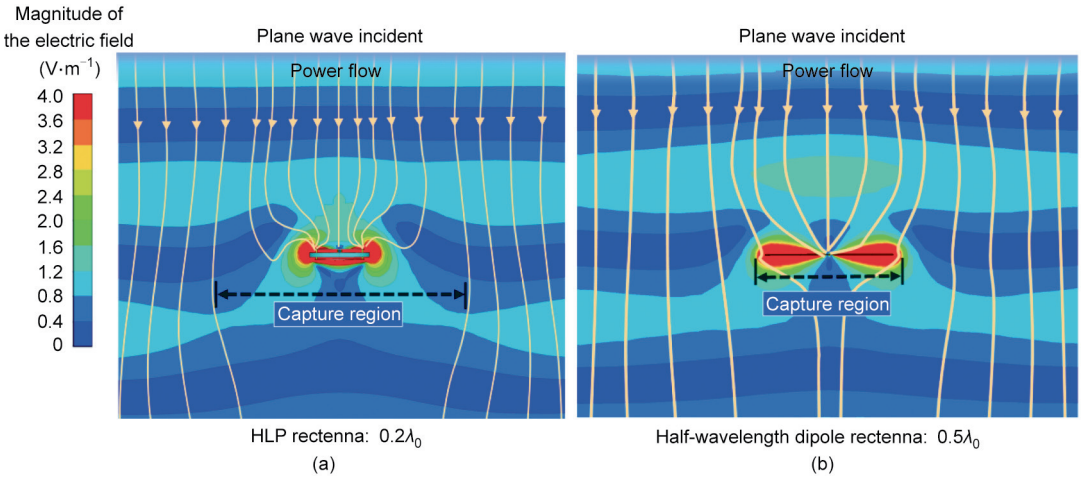

Fig. 13. Comparison of the capacity of a rectenna to capture incident EM-waves. (a) Our developed HLP rectenna; (b) a conventional half-wavelength dipole rectenna.

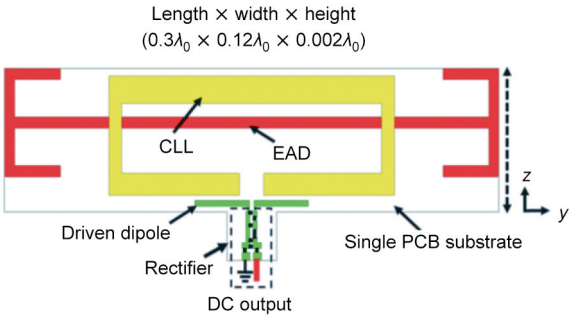

Fig. 14. Configuration of the ultrathin electrically small HLP rectenna realized on a single PCB substrate layer. Reproduced from Ref. [50] with the permission of the IEEE, ©2021.

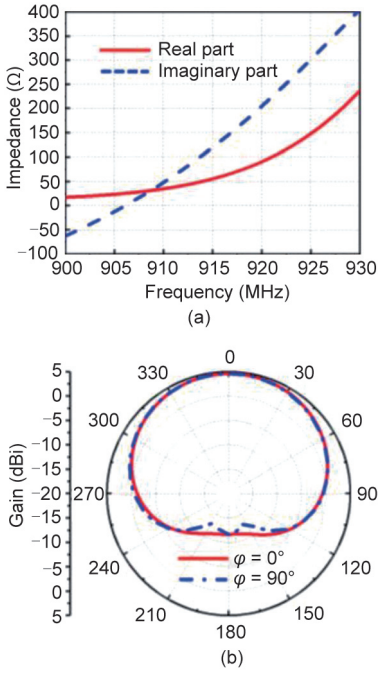

Fig. 15. Simulated performance characteristics of the HLP antenna in the ultrathin rectenna. (a) Input impedance as a function of the source frequency; (b) realized gain patterns at 915 MHz in its two principal vertical planes. Reproduced from Ref. [50] with the permission of the IEEE, ©2021.

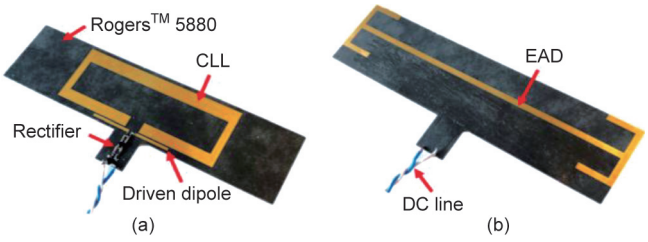

Fig. 16. Fabricated prototype: (a) front view; (b) bottom view. Reproduced from Ref. [50] with the permission of the IEEE, ©2021.

the received power was 10.4 dBm. The efficiency was greater than 50% over a wide range, −4.0–13.0 dBm, of received powers. These results confirm the successful realization of a highly efficient ultrathin HLP rectenna.

4.3. Demonstration of wirelessly powered IoT sensors facilitated by the developed rectennas

Both temperature and light sensors that are wirelessly powered have been developed by integrating them into the developed HLP rectennas. As shown in Fig. 18(a) [51], if the output branch of the rectifier is augmented with an impedance variable sensor, the output DC voltage across the load resistor will be dependent on the sensing parameter. Based on this concept, two wirelessly powered sensor systems (temperature and light level) with threshold alarms have been developed [51]. Fig. 18(b) [51] shows the PCB layout of the sensor-augmented rectifier. It is a simple modification of the previously described rectifier.

Fig. 19(a) [50] shows the low-profile HLP rectenna augmented with the temperature sensor. A thermistor with a negative temperature coefficient from TDK™, Japan (its impedance decreases as the temperature rises) was selected as the temperature sensor. As predicted, the output DC voltage increased when the ambient temperature increased. The DC output is connected to an acoustic siren that has a turn-on voltage of 0.8 V. Thus, the siren is activated if the voltage exceeds the 0.8 V threshold. Fig. 19(b) [50] shows the corresponding ultrathin HLP rectenna augmented with the light sensor. A photocell from Adafruit™, USA was chosen as the light sensor. It is nearly an open-circuit in a dark environment and has a resistance of approximately 1.5 kΩ in a bright setting. As predicted, there is no output DC voltage from the rectenna in a dark environment. On the other hand, the voltage increased

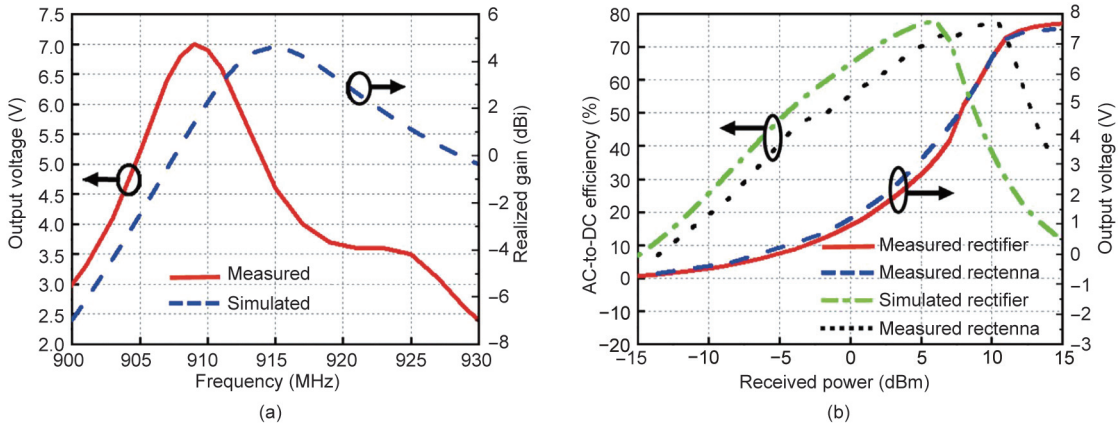

Fig. 17. Ultrathin HLP rectenna performance. (a) Measured output DC voltage and simulated realized gain values as functions of the source frequency; (b) measured and simulated AC-to-DC efficiencies and measured DC output voltages. Reproduced from Ref. [50] with the permission of the IEEE, ©2021.

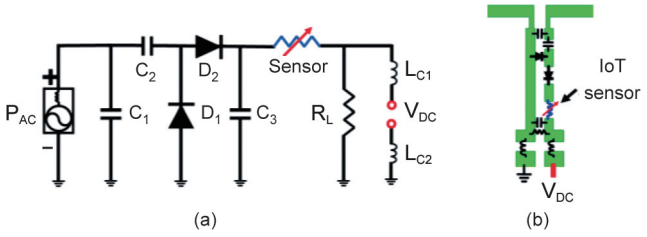

Fig. 18. Configuration of the sensor augmented rectifier [51]. (a) Sensor augmented rectifier. D_1, D_2: HSMS286C Schottky diodes; L_{C1}, L_{C2}: RF chokes. (b) PCB layout.

dramatically when the illumination level increased. The acoustic siren is powered by the rectifier once the threshold has been surpassed. In both cases, the threshold alarm would alert someone to a specified amount of change in the local environment.

Fig. 20 [51] presents the measured output DC voltages for both wirelessly powered sensor systems. As shown in Fig. 20(a) [51], the DC voltage increases when the ambient temperature increases. Once the temperature exceeds 65 °C, the voltage exceeds the 0.8 V threshold and the acoustic siren is activated. This wirelessly powered sensor is suitable, for example, for high-temperature warning applications. Fig. 20(b) [51] indicates that the output DC voltage increases significantly when the ambient illumination level increases. The acoustic siren is inactive in dark environments, but is triggered even under dim light. This wirelessly powered sensor is suitable, for example, for security applications that require an alarm if light is detected in a room.

5. Highly efficient, electrically small HCP rectennas

The HLP rectennas are suitable for applications in which the orientations of the transmitting antenna and the rectenna are known and can be fixed. The polarizations of the transmitter and receiver must be appropriately aligned to achieve the maximum power transfer. If they are not, a resulting polarization mismatch occurs and may significantly degrade the WPT system performance. To address this issue, electrically small HCP rectenna systems have been developed [49,52,53].

As previously described, the HLP antenna design adopted an ED and MD pair excited with an elemental dipole antenna. An HCP antenna can be realized if another ED and MD pair, i.e., another pair of EAD and CLL NFRP elements excited by another elemental dipole, is integrated orthogonal to the first pair and excited with a 90° phase difference. The electromagnetics used in this design is illustrated in Fig. 21 [52]. Two ED and MD pairs (first pair in solid lines; second pair in dashed lines) are arranged in an orthogonal configuration in the *x*–*y* plane. The phase of the second pair is presented as being 90° ahead of the first pair. This clockwise phase advance arrangement of the HLP pairs radiates left hand circularly-polarized (LHCP) fields, and the relative directions of the EDs and MDs produce a circularly-polarized (CP) cardioid

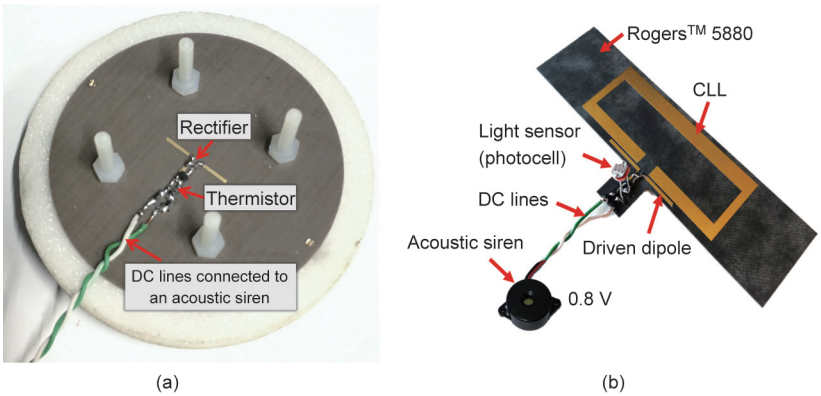

Fig. 19. Wirelessly powered proof-of-concept threshold sensor prototypes. (a) Temperature sensor based on the low-profile HLP rectenna; (b) light sensor based on the ultrathin HLP rectenna. Reproduced from Ref. [50] with the permission of the IEEE, ©2021.

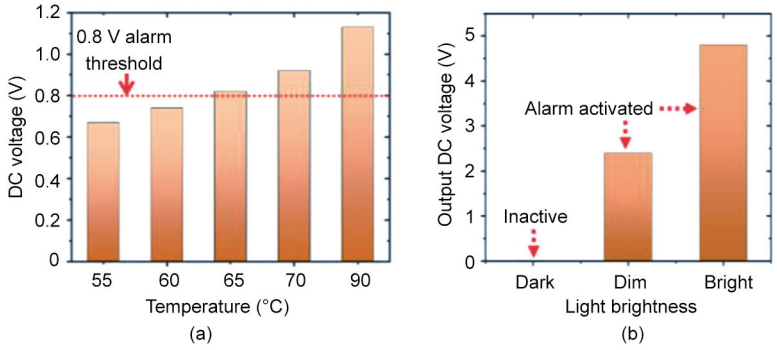

Fig. 20. Measured output DC voltage values for the (a) temperature sensor augmented rectenna, and (b) light sensor augmented rectenna [51].

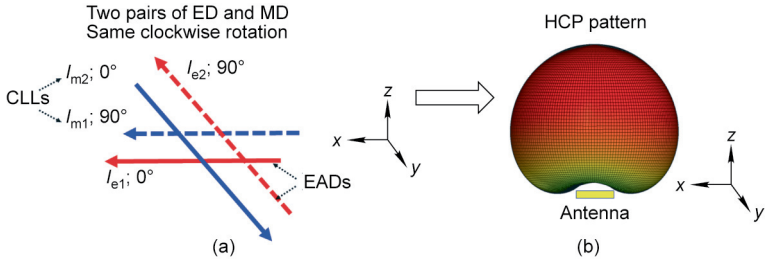

Fig. 21. HCP antenna. (a) Basic EM configuration. I_{e1}, I_{e2}: electric dipole currents; I_{m1}, I_{m2}: magnetic dipole currents. (b) Broadside radiated 3D cardioid pattern. Reproduced from Ref. [52] with the permission of the IEEE, ©2018.

pattern radiated in the broadside direction with its peak along the +z-axis [52]. Based on this concept, two HCP rectenna systems have been developed successfully, i.e., a low-profile unbalanced cross-dipole-based HCP rectenna and a delayed-loop-based HCP rectenna that has the maximum achievable AC-to-DC conversion efficiency.

5.1. Unbalanced cross-dipole HCP rectenna

The low-profile, electrically small, unbalanced cross-dipole-based HCP rectenna [53] is illustrated in Fig. 22(a) [49]. The design evolved straightforwardly from the HLP rectenna as two pairs of the EAD and CLL NFRP elements seamlessly integrated in a cross configuration. It employs the same three Rogers Duroid™ 5880 disks and maintains the same low profile of $0.04\lambda_0$. The requisite 90° phase difference between the resulting two pairs of EDs and MDs is achieved with an unbalanced cross-driven dipole, i.e., by simply introducing a difference in the dipole lengths along the y- and x-axes, l_1 and l_2, as shown in Fig. 22(b) [49]. The rectifier is connected to the cross dipole via an extended 50 Ω co-planar parallel microstrip transmission line. Note that a matching inductor is present because this HCP antenna is matched to the transmission line impedance and not to the rectifier. It is quite difficult to achieve an inductive impedance with this simple unbalanced cross dipole.

Fig. 23 [49] presents the simulated results of the electrically small, unbalanced cross-dipole HCP antenna itself. Fig. 23(a) [49] shows the $|S_{11}|$ and realized gain values as functions of the source frequency. The best CP radiation occurs at 915 MHz which is approximately at the center of its −10 dB impedance bandwidth. The realized LHCP gain is 2.91 dBic and its ka is approximately 0.77 at that frequency. Moreover, the cross-polarized, right hand circularly-polarized (RHCP) levels are significantly lower. The realized gain of the HCP antenna is lower than that of the corresponding HLP antenna because of the greater loss incurred in the substrates owing to the larger fields in them, which are caused by the presence of the additional pair of NFRP elements. The simulated radiation efficiency is 74%. The realized gain patterns at 915 MHz are shown in Fig. 23(b) [49]. Very good Huygens cardioid patterns are realized and are nearly identical in both principal vertical planes. The RHCP cross-polarization levels are substantially lower than the LHCP co-polarization levels.

Fig. 24 [49] presents the measured results of the unbalanced cross-dipole HCP rectenna. The transmitting horn antenna was linearly polarized. Its vertical axis coincided with that of the rectenna. To verify its advantageous CP performance, the rectenna was measured in four different orientations by rotating it with respect to the polarization direction of the horn at four different angles about its vertical axis. Fig. 24(a) [49] shows the measured output DC voltage as a function of the source frequency at those four rotation angles. The best CP performance occurred at 911 MHz, where the received power levels were the closest for all four directions. Thus, the measured operating frequency shifted only 4 MHz (0.4%) from the targeted 915 MHz. Fig. 24(b) [49] shows the measured and simulated AC-to-DC conversion efficiencies at 911 MHz. The

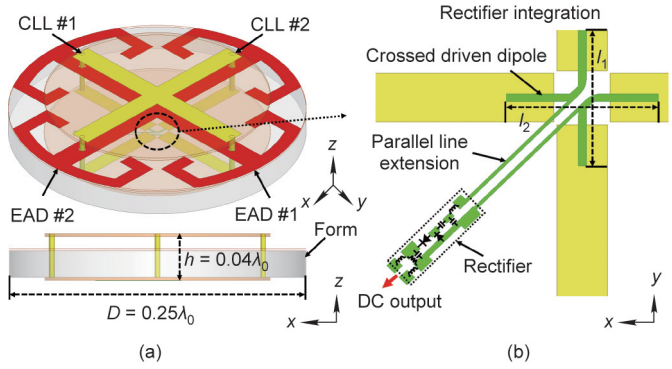

Fig. 22. Low-profile, electrically small, unbalanced cross-dipole HCP rectenna. (a) Entire rectenna model. (b) Details of the rectifier seamlessly integrated with its elemental unbalanced crossed dipole antenna. l_1: the dipole length along the y-axis; l_2: the dipole length along the x-axis. Reproduced from Ref. [49] with the permission of the IEEE, ©2019.

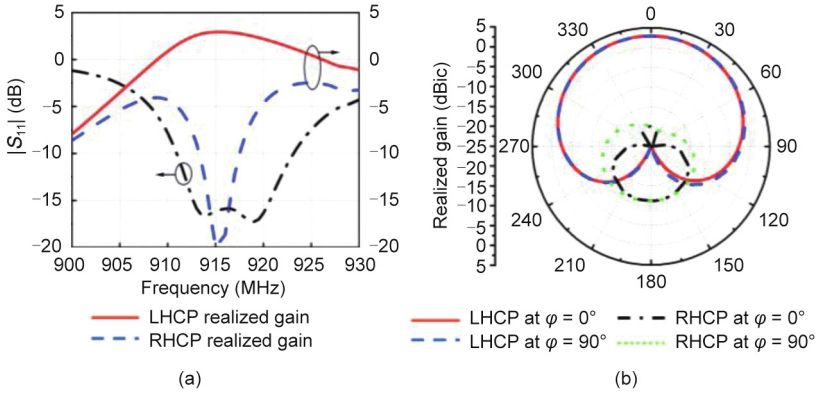

Fig. 23. Simulated performance of the unbalanced cross-dipole HCP antenna alone. (a) $|S_{11}|$ and realized gain values as functions of the source frequency; (b) co-polar (LHCP) and cross-polar (RHCP) realized gain patterns in both principal vertical planes at 915 MHz. RHCP: right hand circularly-polarized. Reproduced from Ref. [49] with the permission of the IEEE, ©2019.

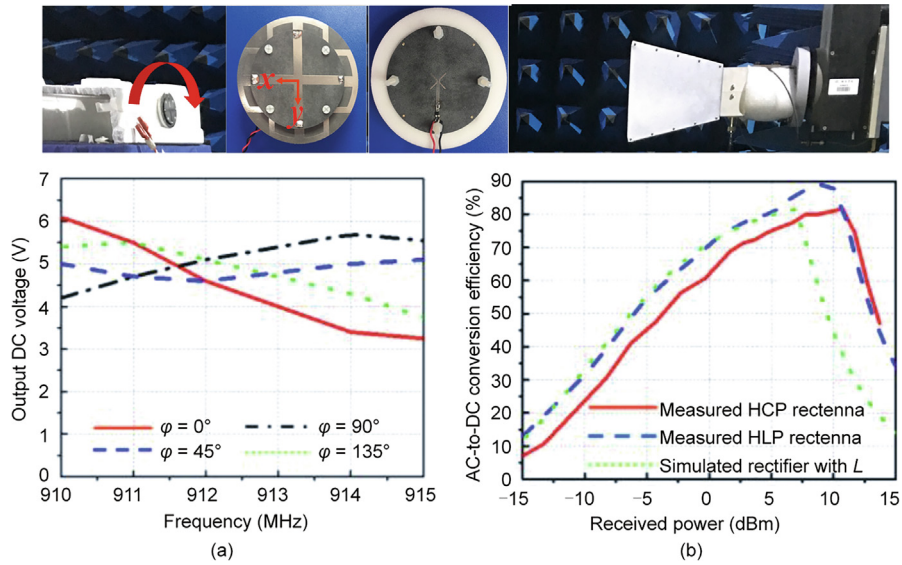

Fig. 24. Measured results of the prototype unbalanced cross-dipole HCP rectenna. (a) Measured output DC voltage as a function of the source frequency when the system is rotated around it vertical axis; (b) measured and simulated AC-to-DC conversion efficiencies at 911 MHz, the frequency at which the best measured CP performance was obtained. Reproduced from Ref. [49] with the permission of the IEEE, ©2019.

AC-to-DC conversion efficiency of the HCP rectenna is 6.9% lower than that of the HLP rectenna because the lossy inductor was required. The peak efficiency was 82% when the received power was 10.7 dBm. As shown, the measured results are very similar to the simulated values of the rectifier circuit, including the lossy inductor, alone.

5.2. Delayed-loop HCP rectenna

The lossy inductor was unavoidable for the unbalanced cross-dipole HCP rectenna. A delayed-loop version was developed to realize an inductive impedance to allow the direct matching of the antenna to the rectifier, while maintaining the HCP cardioid patterns [53]. The configuration of this delayed-loop-based HCP antenna is shown in Fig. 25 [53]. The NFRP elements and their arrangements were the same as the cross-dipole version. The excitation structure consisted of a cross-dipole loaded with two delay loops. Each loop extends from one arm of one driven-dipole arm to one of the orthogonal driven dipole. The parasitic inductance of these loops provides the additional desired inductance to the input impedance of the antenna, as well as the requisite 90° phase difference between the two HLP subsystems to achieve the CP radiation.

Fig. 26(a) [53] presents the simulated input impedance and axial ratio (AR) values of the delayed-loop HCP antenna as functions of the source frequency. The input impedance is (57 + j164) Ω at

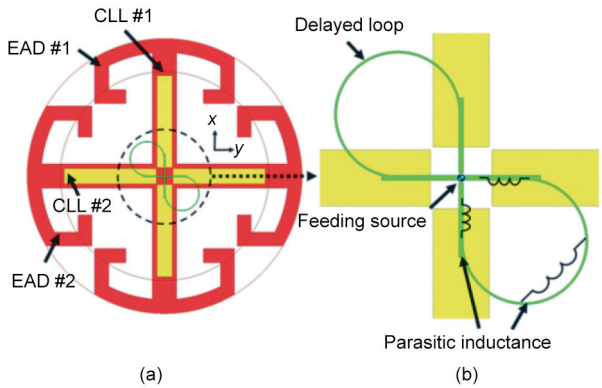

Fig. 25. Delayed-loop HCP antenna. (a) Top view of the model showing the EAD and CLL pairs and the cross-dipole structure loaded with the two delay loops; (b) details of the delayed-loop cross dipole structure. Reproduced from Ref. [53] with the permission of the IEEE, ©2020.

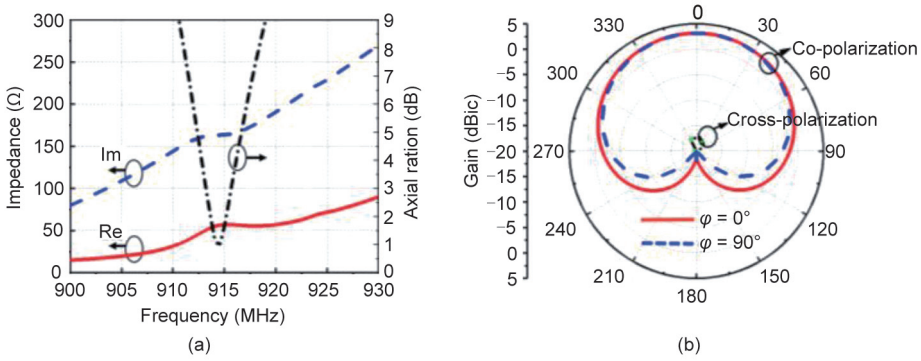

Fig. 26. Simulated performance characteristics of the delayed-loop HCP antenna. (a) Input impedance and axial ratio values as functions of the source frequency. Re: real part; Im: imaginary part; (b) The LHCP (cross-polarization) and RHCP (co-polarization) realized gain patterns at 915 MHz. Reproduced from Ref. [53] with the permission of the IEEE, ©2020.

915 MHz, where the minimum AR value is 1.7 dB, i.e., where the best CP occurs. This impedance allows a direct match to the capacitive rectifier of this system. HCP cardioid realized gain patterns were obtained, as shown in Fig. 26(b) [53]. The system radiates RHCP fields, which is the co-polarization of this system. The LHCP cross-polarization fields were negligible. The peak realized gain is 3.2 dBic and the beamwidth is significantly broad in both principal vertical planes. Its radiation efficiency and FTBR values were 73.1% and 29 dB, respectively. Its *ka* value was approximately 0.77 at 915 MHz.

Fig. 27 [53] presents the fabricated delayed-loop HCP rectenna. An additional piece of the 5880 PCB substrate was required to accommodate the rectifier. It was oriented vertical to the bottom surface of the bottom disk and positioned to make effective contact with the cross-dipole loaded with the delay loops. Plastic blocks and screws were included to support this extra piece. Although the profile of the rectenna increased in comparison to the crossed-dipole-based HCP rectenna because of this extra piece of substrate, the entire prototype remained electrically small with the value of *ka* being approximately 0.77.

Fig. 28(a) [53] presents the measured DC output voltage values as functions of the rotation angle around the rectenna's vertical axis relative to the linear polarization direction of the horn antenna. The best CP performance occurred at 904.5 MHz, where all the output DC voltages were the closest. Thus, the measured operating frequency shifted by 10.5 MHz (1.15%) from the targeted 915 MHz because of the additional structures involved. Fig. 28(b) [53] shows a comparison of the measured and simulated AC-to-DC conversion efficiencies. The efficiency is clearly higher than that of the unbalanced cross-dipole HCP system thanks to the absence of the lossy inductor facilitated by the delay loops and consequent direct match of the antenna to the rectifier. The peak AC-to-DC efficiency reached 90.6%, which was 8.8% higher. The measured results confirmed that the electrically small, delayed-loop HCP rectenna attained the maximum achievable AC-to-DC conversion efficiency.

6. Electrically small, dual-function (WPT and communications) Huygens antenna

Dual-functional antenna systems that enable both WPT and communications are attractive for the emerging SWIPT applications [63]. Nodes in a wirelessly powered sensor network are one such application. Both information signals and power must be delivered between the transmitter/gateway of the sensor ecosystem and its nodes.

Fig. 29(a) [54] illustrates the conceptual design of the dual-functional Huygens antenna system. It is facilitated by the electrically small HCP design. Similar to the HCP antenna configuration, two HLP elements are arranged orthogonal to each other. As indicated, HLP antenna #1 provides the WPT function and HLP antenna #2 provides the communications function. Moreover, because of their orthogonal arrangement, Fig. 29(b) [54] indicates that the isolation between the two systems is excellent. Consequently, these two systems perform their functions independently.

The actual system design is shown in Fig. 30 [54]. In contrast to the single function HLP rectenna but similar to the delayed-loop HCP rectenna, it requires an additional piece of the 5880 PCB substrate. One side of the substrate supports the rectifier for the WPT mode (Port #2), while the other side supports the transmission lines for connection to the communications electronics (Port #1). The entire structure remains compact and electrically small with its *ka* value being approximately 0.77.

Fig. 31(a) [54] shows a photo of the tested electrically small, dual-function Huygens antenna prototype. Fig. 31(b) [54] presents the measured and simulated $|S_{11}|$ and realized gain values as functions of the source frequency for its antenna mode. The measured resonance frequency was 910 MHz, which is a shift of only 5 MHz (0.5%) from the targeted 915 MHz. The measured peak realized gain value was 2.7 dBi, which was also reasonably close to its simulated value of 2.87 dBi. Fig. 32(a) [54] presents the simulated and measured realized gain patterns for the antenna mode at its measured resonance frequency. The cross-polarization levels were significantly lower than the corresponding co-polarization values. High-quality Huygens cardioid patterns were observed in both principal vertical planes. Once again, the measured FTBR was large at 28.8 dB. These measured and simulated results were also in reasonable agreement.

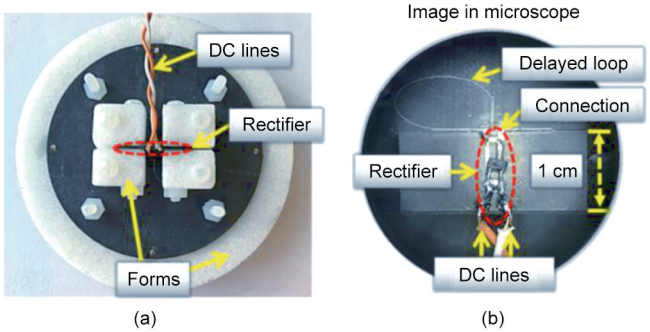

Fig. 27. Bottom views of the measured prototype of the delayed-loop HCP rectenna: (a) visual image; (b) microscope image. Reproduced from Ref. [53] with the permission of the IEEE, ©2020.

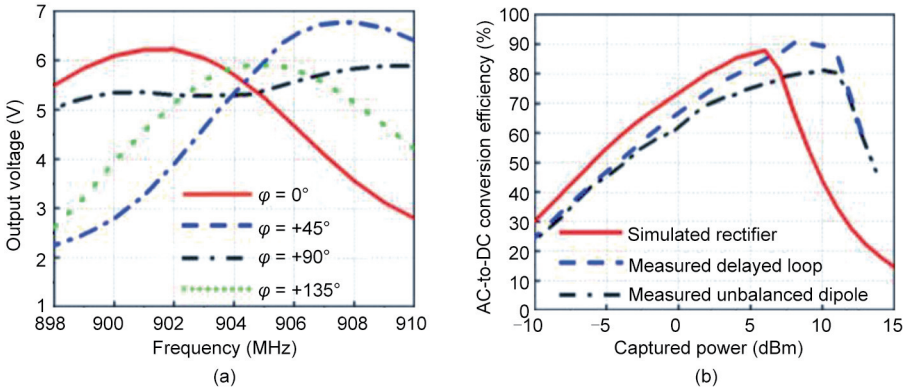

Fig. 28. Measured results of the delayed-loop HCP rectenna. (a) Measured DC output voltage values as functions of the source frequency for different rotation angles around the rectenna's vertical axis relative to the linear polarization direction of the horn antenna; (b) comparison of the measured and simulated AC-to-DC conversion efficiencies. Reproduced from Ref. [53] with the permission of the IEEE, ©2020.

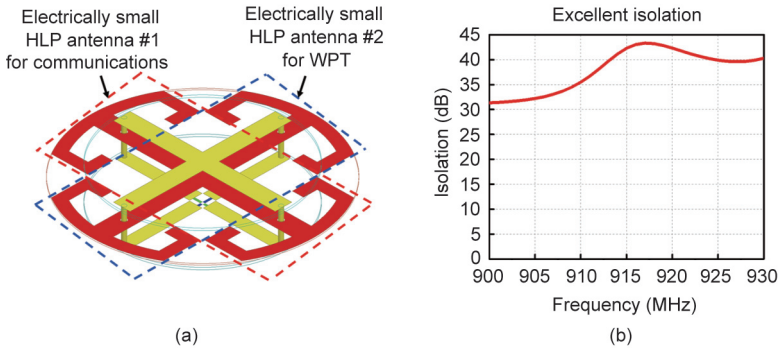

Fig. 29. Design concept of the dual-function electrically small Huygens antenna system. (a) Orthogonal HLPs, one for the WPT and the other one for the communications function; (b) isolation level between the two HLP systems as a function of the source frequency. Reproduced from Ref. [54] with the permission of the IEEE, ©2019.

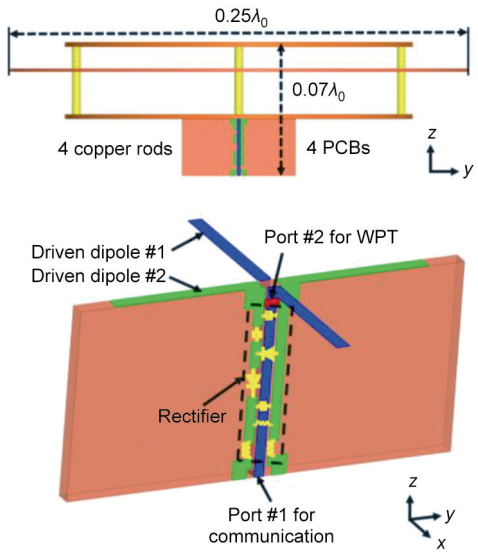

Fig. 30. Electrically small, dual-function Huygens antenna system configuration. Reproduced from Ref. [54] with the permission of the IEEE, ©2019.

The measured and simulated WPT mode performance results are presented in Fig. 32(b) [54]. They also reasonably agree with each other. The measured peak AC-to-DC conversion efficiency was 87.2%; the simulated value was 87.8%, which was only a 0.57% difference. The measured results confirmed the performance characteristics of the simulated electrically small, dual-function Huygens antenna.

7. Ultrathin linear uniform Huygens rectenna arrays

All the rectenna designs described thus far have been single-element systems with only one DC output. Although these single-element systems are highly efficient and have a large wireless power capture capacity, the overall power they receive is effectively limited by their electrically small sizes. To further increase the captured wireless power, a multi-element rectenna array is required.

Rectenna arrays have been realized mainly with two power-combining approaches [64,65]. Their performance characteristics are different and are dependent on both the number of antenna elements and the rectification topology. The best choice is the one that will meet the requirements for a specific application scenario. For example, a rectenna array with a DC combining topology is an incoherent scheme that relies on the gain, beamwidth, and AC-to-DC conversion efficiency of each individual rectenna. The total DC output of the system is a summation of the DC yield of the individual elements. Thus, if the array has N identical HLP rectennas, the ideal output of the system will be N times that of each one. Because of the large beamwidths of each element, it is most suited to environments in which the EM waves are incident on the array from multiple directions.

Alternatively, a rectenna array with an RF combining topology is a coherent approach that relies on its antenna array to form a highly directive beam. The received power is enhanced by the resulting higher gain and is channeled to a single rectifier because

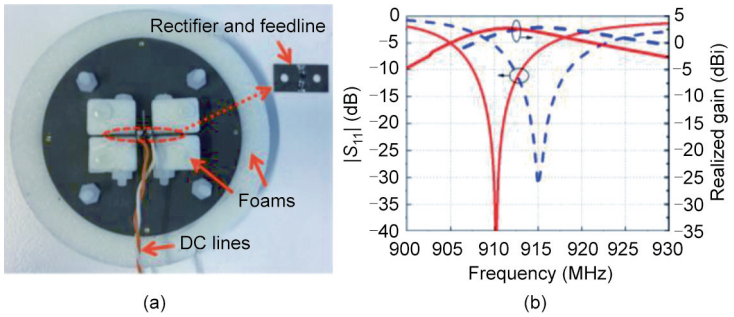

Fig. 31. Dual-function Huygens antenna prototype. (a) Bottom view; (b) measured and simulated $|S_{11}|$ and realized gain values as functions of the source frequency for the communications mode. Reproduced from Ref. [54] with the permission of the IEEE, ©2019.

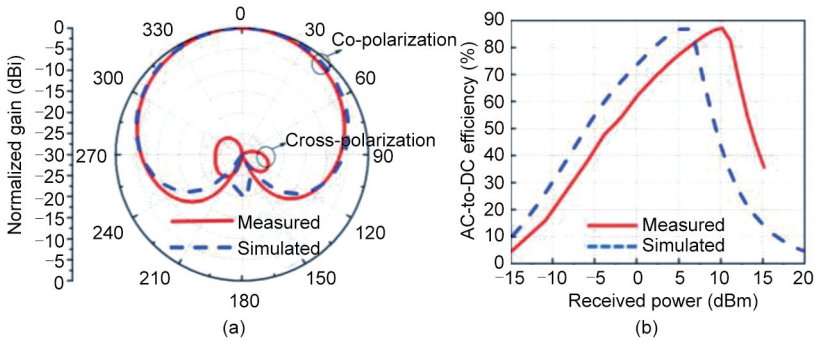

Fig. 32. Dual-function Huygens antenna prototype. (a) Simulated and measured normalized realized gain patterns at its measured resonance frequency; (b) measured and simulated WPT mode performance. Reproduced from Ref. [54] with the permission of the IEEE, ©2019.

it is a nonlinear element that operates more efficiently at higher power levels. An ideal array of N in-phase HLP antennas has a gain and, hence, a received power that is approximately N times that of the individual element. Consequently, this RF topology is most suited to situations in which the transmitter beacon has a low power and its location is fixed and known. If it is not fixed, there will be a power cost associated with the need to energize a control unit that must track the transmitter and create the phase shifts necessary to steer the beam of the rectenna array towards it.

7.1. Huygens rectenna array with a DC combining topology

An ultrathin rectenna array is readily achieved with a DC combining topology [66]. Assuming the array to be linear and uniform, N ultrathin electrically small HLP rectennas can be arranged along a line with a uniform distance between their centers. This concept is illustrated with four ultrathin HLP rectennas arranged along the y-axis with a $0.45\lambda_0$ spacing between their centers, as shown in Fig. 33. The DC outputs of all of the HLP rectennas are connected in a parallel configuration. Therefore, the total DC output current is the sum of the currents obtained from each output port of the four rectifiers. Note that a series arrangement is also possible and would yield the sum of the output voltages.

With the advantage of the very broad beamwidth performance of each HLP rectenna, this array is able to efficiently capture EM waves incident on it from any direction in the $+z$ hemisphere. Another notable feature of the DC combining topology is that the output current can be enhanced for applications that require more driven-current simply by adding more elements. Because the scheme is based on each rectenna being essentially an independent entity, an ideal system of N identical elements would yield N times the output of each. Moreover, because the HLP rectennas are

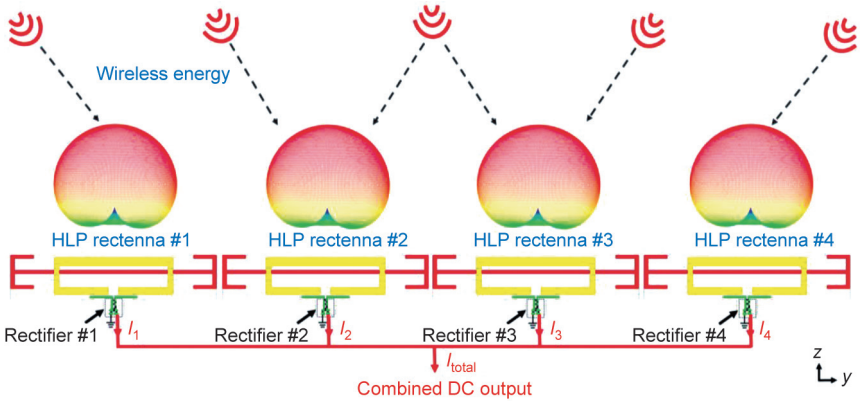

Fig. 33. Linear uniform Huygens rectenna array with DC combining topology. I_1, I_2, I_3, I_4: the current obtained from the output port of rectifier 1, 2, 3, and 4, respectively; I_{total}: the total DC output current.

electrically small, many more of them can fit into a specified region of restricted size. Hence, an array of these electrically small elements in a fixed footprint will yield a larger output as compared to having a restricted number of standard resonant half-wavelength elements. Fig. 34 presents the simulated radiation patterns of the four receiving HLP antennas when they are matched to 50 Ω loads. It is clear that the mutual interference between these elements is relatively minor and acceptable Huygens cardioid patterns are realized by all four HLP antennas. Consequently, much larger wireless power capture capacity is demonstrated.

7.2. Huygens rectenna array with an RF combining topology

The corresponding rectenna array with an RF combining topology is shown in Fig. 35. In contrast to the DC combining topology, where each HLP receiving antenna is connected to its own rectifier, the entire array is connected to only one rectifier via a feed network. In this manner, the output power from each element is combined in the RF domain. The input power delivered to the rectifier by the feed network is thus higher; therefore, its diode can operate more efficiently.

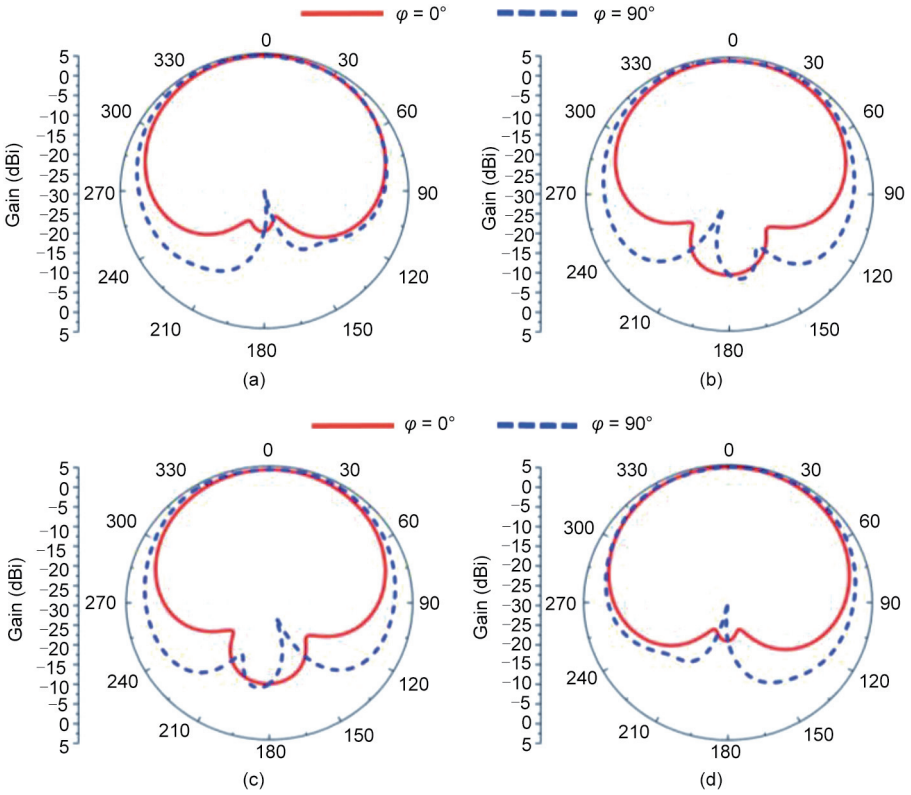

Fig. 34. Simulated realized gain patterns at 915 MHz of each of the electrically small, ultrathin HLP antennas in a 1 × 4 linear array: (a) HLP antenna #1; (b) HLP antenna #2; (c) HLP antenna #3; (d) HLP antenna #4.

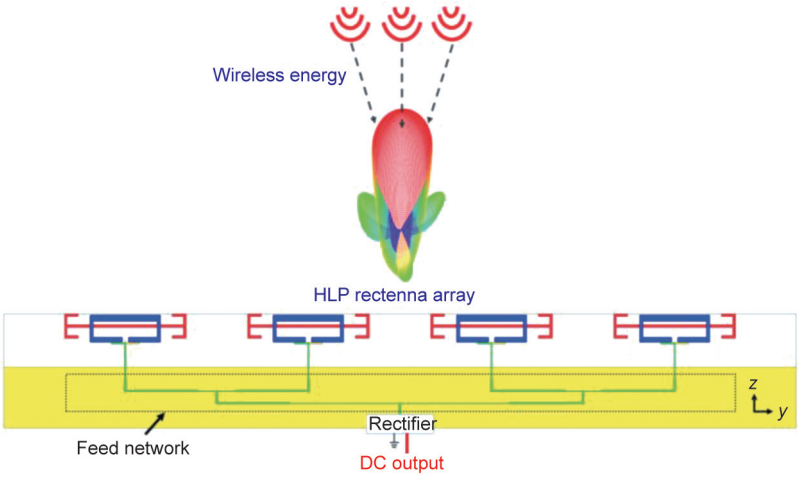

Fig. 35. Linear uniform Huygens rectenna array with RF combining topology.

Consider the array of the WPT system illustrated in Fig. 35 first as a transmitter. The radiated broadside beam of the array with each element excited with the same amplitude and phase has a narrow beamwidth in the principal vertical plane along the array and a significantly broad beamwidth in the orthogonal plane, as shown in Fig. 36. Consequently, the receiving version of this array would then be more suitable for collecting power within a narrow angular range, i.e., around its broadside direction, in that principal plane. Significantly low received power levels are expected for EM waves arriving from other angles in that plane, particularly from low elevation angles. The simulated realized gain patterns of the corresponding four-element receiving HLP antenna array that is matched to a single 50 Ω source through the microstrip feedline network shown in Fig. 35 are the same as those presented in Fig. 36. The array has a notably broad beamwidth (134° from −66° to 68°) in its H-plane (φ = 0°, z–x plane), and a narrow beamwidth (28° from −13° to 15°) in its E-plane (φ = 90°, y–z plane). Nevertheless, the maximum realized gain, 9.5 dBi, is the same in the broadside direction in both planes indicating that the system still provides a significant EM-wave power capture capability. Thus, a significantly enhanced level of received power is available to be delivered to the rectifier of the system.

Prototypes of these ultrathin linear uniform HLP rectenna arrays with both combining topologies are currently being optimized for fabrication and measurement. Planar arrays of $N \times M$ elements are also being considered to further enhance the outputs of both systems for a variety of applications.

8. Conclusions

Far-field WPT is a critical technology for the realization of the many anticipated ubiquitous IoT applications associated with 5G, 6G, and beyond wireless ecosystems. The rectenna is the most critical component of any far-field WPT system. The development of a series of high performance electrically small, Huygens rectennas was described. Both HLP and HCP rectenna systems were presented. These HLP and HCP rectennas were realized with metamaterial-inspired NFRP elements and elemental dipole antennas seamlessly combined with compact, highly efficient rectifiers.

The low-profile HLP rectenna was realized as a three-layer structure. The ultrathin HLP rectenna was realized using a single substrate layer. AC-to-DC conversion efficiencies of nearly 90% were realized with both systems. The modification of both HLP rectennas to achieve wirelessly powered temperature and light sensor threshold warning systems was described. By combining two HLP subsystems in an orthogonal arrangement with the requisite phase difference of 90°, HCP rectennas were also demonstrated. The first type was realized with the same three-layer low-profile design as employed in the corresponding HLP system. Its two HLP subsystems were integrated with an unbalanced cross-dipole antenna to attain the necessary 90° phase difference. Its AC-to-DC conversion efficiency is limited by this simple cross-dipole element. The maximum AC-to-DC conversion efficiency was greater than 90% and was achieved by replacing the unbalanced cross dipole with an innovative delayed-loop version. Having realized that the orthogonal HLP elements are highly isolated from each other, a dual-functional HLP system was developed for SWIPT applications. One HLP subsystem performed the WPT function; the other performed the communications function.

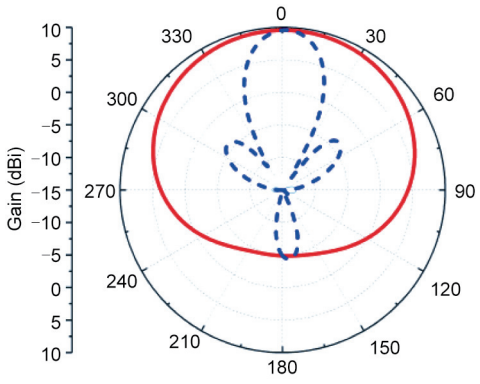

Fig. 36. Simulated realized gain patterns at 915 MHz of the four-element linear uniform HLP antenna array that is fed by the microstrip feedline connected a single master source.

Finally, two linear uniform rectenna arrays formed with four identical ultrathin, electrically small HLP rectennas were considered to demonstrate a larger EM-wave capture capacity. The arrays were integrated with both DC and RF combining topologies. The elements acted independently in the DC system, and their individual DC outputs were connected in a parallel arrangement to produce a large combined current at its output port. The elements were combined in phase in the RF system to produce a directive beam that would point towards a low-power WPT beacon to capture its EM waves, efficiently forming a large combined power that would be delivered to its single rectifier.

The developed electrically small Huygens rectennas and the linear arrays formed with them are ideal candidates for wirelessly powered IoT applications in future wireless ecosystems. Their unidirectional, broadside radiated fields effectuate immediate, significant advantages over typically employed, conventional ED systems. Moreover, as demonstrated, they are compact in size, have large and broad-angle wireless power capture capabilities, have high AC-to-DC conversion efficiencies, and are easy to fabricate at low costs.

Acknowledgments

The authors would like to thank Professor Jianquan Huang from Xiangnan University for his assistance with the measurement campaigns; and Professor Yingjie Jay Guo from University of Technology Sydney for his support of these efforts.

This work was supported by the University of Technology Sydney (UTS) Chancellor's Postdoctoral Fellowship (PRO18-6147) and Australian Research Council (ARC) Discovery Early Career Researcher Award (DECRA) (PRO20-9959).

Compliance with ethics guidelines

Wei Lin and Richard W. Ziolkowski declare that they have no conflict of interest or financial conflicts to disclose.

References

[1] Tesla N, inventor. Apparatus for transmitting electrical energy. United States patent US 1119732. 1914 Dec 1.
[2] Tesla N. The true wireless. Electr Exp 1919;2(5):1–13.
[3] Wheeler LP. II—Tesla's contribution to high frequency. Electr Eng 1943;62(8):355–7.
[4] Brown WC. The history of power transmission by radio waves. IEEE Trans Microw Theory Tech 1984;32(9):1230–42.
[5] Matsumoto H. Research on solar power satellites and microwave power transmission in Japan. IEEE Microw Mag 2002;3(4):36–45.
[6] Dickinson RM. Power in the sky: requirements for microwave wireless power beamers for powering high-altitude platforms. IEEE Microw Mag 2013;14(2):36–47.
[7] Strassner B, Chang K. Microwave power transmission: historical milestones and system components. Proc IEEE 2013;101(6):1379–96.
[8] Massa A, Oliveri G, Viani F, Rocca P. Array designs for long-distance wireless power transmission: state-of-the-art and innovative solutions. Proc IEEE 2013;101(6):1464–81.

[9] Costanzo A, Dionigi M, Masotti D, Mongiardo M, Monti G, Tarricone L, et al. Electromagnetic energy harvesting and wireless power transmission: a unified approach. Proc IEEE 2014;102(11):1692–711.
[10] Carvalho NB, Georgiadis A, Costanzo A, Rogier H, Collado A, García JA, et al. Wireless power transmission: R&D activities within Europe. IEEE Trans Microw Theory Tech 2014;62(4):1031–45.
[11] Costanzo A, Masotti D. Smart solutions in smart spaces: getting the most from far-field wireless power transfer. IEEE Microw Mag 2016;17(5):30–45.
[12] Popovic Z. Near- and far-field wireless power transfer. In: Proceedings of 2017 13th International Conference on Advanced Technologies, Systems and Services in Telecommunications (TELSIKS); 2017 Oct 18–20; Nis, Serbia; 2017. p. 3–6.
[13] Hester JGD, Kimionis J, Tentzeris MM. Printed motes for IoT wireless networks: state of the art, challenges, and outlooks. IEEE Trans Microw Theory Tech 2017;65(5):1819–30.
[14] Costanzo A, Masotti D. Energizing 5G: near- and far-field wireless energy and data transfer as an enabling technology for the 5G IoT. IEEE Microw Mag 2017;18(3):125–36.
[15] Wagih M, Weddell AS, Beeby S. Rectennas for radio-frequency energy harvesting and wireless power transfer: a review of antenna design. IEEE Antennas Propag Mag 2020;62(5):95–107.
[16] Shinohara N. History and innovation of wireless power transfer via microwaves. IEEE J Microw 2021;1(1):218–28.
[17] Li L, Zhang X, Song C, Huang Y. Progress, challenges, and perspective on metasurfaces for ambient radio frequency energy harvesting. Appl Phys Lett 2020;116(6):060501.
[18] Surender D, Khan T, Talukdar FA, De A, Antar YMM, Freundorder AP. Key components of rectenna system: a comprehensive survey. IETE J Res. In press.
[19] Campi T, Cruciani S, Palandrani F, De Santis V, Hirata A, Feliziani M. Wireless power transfer charging system for AIMDs and pacemakers. IEEE Trans Microw Theory Tech 2016;64(2):633–42.
[20] Jadidian J, Katabi D. Magnetic MIMO: how to charge your phone in your pocket. In: Proceedings of the 20th Annual International Conference on Mobile Computing and Networking; 2014 Sep 7–11; Maui, HI, USA; 2014. p. 495–506.
[21] Karalis A, Joannopoulos JD, Soljačić M. Efficient wireless non-radiative mid-range energy transfer. Ann Phys 2008;323(1):34–48.
[22] Schormans M, Valente V, Demosthenous A. Frequency splitting analysis and compensation method for inductive wireless powering of implantable biosensors. Sensors 2016;16(8):1229.
[23] McSpadden JO, Mankins JC. Space solar power programs and microwave wireless power transmission technology. IEEE Microw Mag 2002;3(4):46–57.
[24] Talla V, Kellogg B, Gollakota S, Smith JR. Battery-free cellphone. Proc ACM Interact Mob Wearable Ubiquitous Technol 2017;1(2):1–20.
[25] Misra V, Bozkurt A, Calhoun B, Jackson T, Jur J, Lach J, et al. Flexible technologies for self-powered wearable health and environmental sensing. Proc IEEE 2015;103(4):665–81.
[26] Palazzi V, Hester J, Bito J, Alimenti F, Kalialakis C, Collado A, et al. A novel ultra-lightweight multiband rectenna on paper for RF energy harvesting in the next generation LTE bands. IEEE Trans Microw Theory Tech 2018;66(1):366–79.
[27] Shen S, Chiu CY, Murch RD. Multiport pixel rectenna for ambient RF energy harvesting. IEEE Trans Antennas Propag 2018;66(2):644–56.
[28] Sun H, Guo Y, He M, Zhong Z. Design of a high-efficiency 2.45-GHz rectenna for low-input-power energy harvesting. IEEE Antennas Wirel Propag Lett 2012;11:929–32.
[29] Popovic Z, Falkenstein EA, Costinett D, Zane R. Low-power far-field wireless powering for wireless sensors. Proc IEEE 2013;101(6):1397–409.
[30] Yang Y, Li J, Li L, Liu Y, Zhang B, Zhu H, et al. A 5.8 GHz circularly polarized rectenna with harmonic suppression and rectenna array for wireless power transfer. IEEE Antennas Wirel Propag Lett 2018;17(7):1276–80.
[31] Sun H, Geyi W. A new rectenna using beamwidth-enhanced antenna array for RF power harvesting applications. IEEE Antennas Wirel Propag Lett 2017;16:1451–4.
[32] Li L, Zhang X, Song C, Zhang W, Jia T, Huang Y. Compact dual-band, wide-angle, polarization-angle-independent rectifying metasurface for ambient energy harvesting and wireless power transfer. IEEE Trans Microw Theory Tech 2021;69(3):1518–28.
[33] Zhang X, Liu H, Li L. Tri-band miniaturized wide-angle and polarization-insensitive metasurface for ambient energy harvesting. Appl Phys Lett 2017;111(7):071902.
[34] Ho DK, Ngo VD, Kharrat I, Vuong TP, Nguyen QC, Le MT. A novel dual-band rectenna for ambient RF energy harvesting at GSM 900 MHz and 1800 MHz. Adv Sci Technol Eng Syst J 2017;2(3):612–6.
[35] Zeng M, Andrenko AS, Liu X, Li Z, Tan HZ. A compact fractal loop rectenna for RF energy harvesting. IEEE Antennas Wirel Propag Lett 2017;16:2424–7.
[36] Shi Y, Jing J, Fan Y, Yang L, Wang M. Design of a novel compact and efficient rectenna for WiFi energy harvesting. Prog Electromagn Res C 2018;83:57–70.
[37] Liu C, Guo YX, Sun H, Xiao S. Design and safety considerations of an implantable rectenna for far-field wireless power transfer. IEEE Trans Antennas Propag 2014;62(11):5798–806.
[38] Zhu N, Ziolkowski RW, Xin H. A metamaterial-inspired, electrically small rectenna for high-efficiency, low power harvesting and scavenging at the global positioning system L1 frequency. Appl Phys Lett 2011;99(11):114101.
[39] Gu X, Hemour S, Guo L, Wu K. Integrated cooperative ambient power harvester collecting ubiquitous radio frequency and kinetic energy. IEEE Trans Microw Theory Tech 2018;66(9):4178–90.
[40] Hosain MK, Kouzani AZ, Tye SJ, Abulseoud OA, Amiet A, Galehdar A, et al. Development of a compact rectenna for wireless powering of a head-mountable deep brain stimulation device. IEEE J Transl Eng Health Med 2014;2:1–13.
[41] Quddious A, Zahid S, Tahir FA, Antoniades MA, Vryonides P, Nikolaou S. Dual-band compact rectenna for UHF and ISM wireless power transfer systems. IEEE Trans Antennas Propag 2021;69(4):2392–7.
[42] Eid A, Hester JGD, Costantine J, Tawk Y, Ramadan AH, Tentzeris MM. A compact source–load agnostic flexible rectenna topology for IoT devices. IEEE Trans Antennas Propag 2020;68(4):2621–9.
[43] Hoefle M, Haehnsen K, Oprea I, Cojocari O, Penirschke A, Jakoby R. Compact and sensitive millimetre wave detectors based on low barrier Schottky diodes on impedance matched planar antennas. J Infrared Millim Terahertz Waves 2014;35(11):891–908.
[44] Chuma EL, Rodríguez LDLT, Iano Y, Roger LLB, Sanchez-Soriano MA. Compact rectenna based on a fractal geometry with a high conversion energy efficiency per area. IET Microw Antennas Propag 2018;12(2):173–8.
[45] Shrestha S, Lee SR, Choi DY. A new fractal-based miniaturized dual band patch antenna for RF energy harvesting. Int J Antennas Propag 2014;2014:1–9.
[46] Bakogianni S, Koulouridis S. A dual-band implantable rectenna for wireless data and power support at sub-GHz region. IEEE Trans Antennas Propag 2019;67(11):6800–10.
[47] Cheng HW, Yu TC, Luo CH. Direct current driving impedance matching method for rectenna using medical implant communication service band for wireless battery charging. IET Microw Antennas Propag 2013;7(4):277–82.
[48] Tang MC, Wang H, Ziolkowski RW. Design and testing of simple, electrically small, low-profile, Huygens source antennas with broadside radiation performance. IEEE Trans Antennas Propag 2016;64(11):4607–17.
[49] Lin W, Ziolkowski RW, Huang J. Electrically small, low profile, highly efficient, Huygens dipole rectennas for wirelessly powering Internet-of-Things (IoT) devices. IEEE Trans Antennas Propag 2019;67(6):3670–9.
[50] Lin W, Ziolkowski RW. Electrically small, single-substrate Huygens dipole rectenna for ultracompact wireless power transfer applications. IEEE Trans Antennas Propag 2021;69(2):1130–4.
[51] Lin W, Ziolkowski RW. Wirelessly powered light and temperature sensors facilitated by electrically small omnidirectional and Huygens dipole antennas. Sensors 2019;19(9):1998.
[52] Lin W, Ziolkowski RW. Electrically-small, low-profile, Huygens circularly polarized antenna. IEEE Trans Antennas Propag 2018;66(2):636–43.
[53] Lin W, Ziolkowski RW. Electrically small Huygens CP rectenna with a driven loop element maximizes its wireless power transfer efficiency. IEEE Trans Antennas Propag 2020;68(1):540–5.
[54] Lin W, Ziolkowski RW. Electrically small Huygens antenna-based fully-integrated wireless power transfer and communication system. IEEE Access 2019;7:39762–9.
[55] Luk KM, Wong H. A new wideband unidirectional antenna element. Int J Microw Opt Technol 2006;1(1):35–44.
[56] Ge L, Luk KM. A low-profile magneto-electric dipole antenna. IEEE Trans Antennas Propag 2012;60(4):1684–9.
[57] Luk KM, Wu B. The magnetoelectric dipole—a wideband antenna for base stations in mobile communications. Proc IEEE 2012;100(7):2297–307.
[58] Wang J, Li Y, Wang J, Ge L, Chen M, Zhang Z, et al. A low-profile vertically polarized magneto-electric monopole antenna with a 60% bandwidth for illimetre-wave applications. IEEE Trans Antennas Propag 2020;69(1):3–13.
[59] Li Y, Ge L, Chen M, Zhang Z, Li Z, Wang J. Multibeam 3-D-printed illimet lens fed by magnetoelectric dipole antennas for illimetre-wave MIMO applications. IEEE Trans Antennas Propag 2019;67(5):2923–33.
[60] Ziolkowski RW. Using Huygens multipole arrays to realize unidirectional needle-like radiation. Phys Rev X 2017;7(3):031017.
[61] Ziolkowski RW. Low profile, broadside radiating, electrically small Huygens source antennas. IEEE Access 2015;3:2644–51.
[62] Balanis CA. Antenna theory: analysis and design. 3rd ed. New York City: John Wiley & Sons; 2005.
[63] Ponnimbaduge Perera TD, Jayakody DNK, Sharma SK, Chatzinotas S, Li J. Simultaneous wireless information and power transfer (SWIPT): recent advances and future challenges. IEEE Commun Surv Tutor 2018;20(1):264–302.
[64] Olgun U, Chen CC, Volakis JL. Investigation of rectenna array configurations for enhanced RF power harvesting. IEEE Antennas Wirel Propag Lett 2011;10:262–5.
[65] Lee DJ, Lee SJ, Hwang IJ, Lee WS, Yu JW. Hybrid power combining rectenna array for wide incident angle coverage in RF energy transfer. IEEE Trans Microw Theory Tech 2017;65(9):3409–18.
[66] Parks AN, Smith JR. Sifting through the airwaves: efficient and scalable multiband RF harvesting. In: Proceedings of 2014 IEEE International Conference on RFID; 2014 Apr 8–10; Orlando, FL, USA; 2014. p. 74–81.